

## Article

# Petrogenesis of the Eocene Highly Fractionated Granite Porphyry with REE Tetrad Effect: An Example from Western Yunnan, Southeastern Tibetan Plateau

Hang Yang <sup>1</sup>, Peng Wu <sup>1,\*</sup>, Anlin Liu <sup>1,\*</sup> and Feng Wang <sup>1,2</sup>

<sup>1</sup> Faculty of Land Resource Engineering, Kunming University of Science and Technology, Kunming 650093, China; yanghang19941225@163.com (H.Y.); wfwj@vip.163.com (F.W.)

<sup>2</sup> Yunnan Metallurgy Resources Exploration Co., Ltd., Kunming 651100, China

\* Correspondence: wupeng8104@kmust.edu.cn (P.W.); anlinliu@kust.edu.cn (A.L.)

**Abstract:** Highly fractionated granites are widely distributed in the crust and provide unique windows into magmatic evolution. This study reports petrography, zircon U–Pb ages, trace elemental, and Hf isotopic, as well as whole-rock elemental and Nd isotopic data of highly fractionated granite porphyries from the Shiguanshan area in western Yunnan, southeastern Tibet. The granite porphyries were formed at  $34.0 \pm 0.3$  Ma in a post-collisional setting. They are strongly peraluminous ( $A/CNK = 1.95\text{--}2.80$ ), have high  $\text{SiO}_2$  content ( $\text{SiO}_2 = 78.16\text{--}79.13$  wt.%) and zircon saturation temperatures ( $803\text{--}829$  °C, average  $819$  °C), and low MgO, with pronounced enrichment in Pb, U, Th, and Rb, and depletion in Ti, Eu, P, Sr, and Ba, and belong to highly fractionated A-type granites. These rocks define linear trends on Harker diagrams and display similar enriched whole-rock Nd isotopic ( $\epsilon_{\text{Nd}}(t) = -12.8$  to  $-12.3$ ) and zircon Hf isotopic ( $\epsilon_{\text{Hf}}(t) = -10.4$  to  $-8.8$ ) compositions compared to the published data of coeval mantle-derived syenite porphyries, which can be attributed to fractional crystallization processes. A quantitative model suggests that the Shiguanshan granite porphyries likely formed through the fractionation process of a mineral assemblage consisting of plagioclase, K-feldspar, biotite, and amphibole (in a ratio of 40:30:25:5), with fractionation degrees of 50%–55%. The magmatic textures and zircons, decoupling between the REE tetrad effect and fractionation of twin-elements, along with the modeling result of Rayleigh fractionation, suggest that the REE tetrad effect in the Shiguanshan granite porphyries may be caused by fractionation of accessory minerals. Our data, along with regional observations, propose that the generation of these granite porphyries is possibly related to lithospheric removal following the Indo–Asia collision.

**Keywords:** highly fractionated granite porphyry; REE tetrad effect; fractional crystallization; western Yunnan; southeastern Tibet



**Citation:** Yang, H.; Wu, P.; Liu, A.; Wang, F. Petrogenesis of the Eocene Highly Fractionated Granite Porphyry with REE Tetrad Effect: An Example from Western Yunnan, Southeastern Tibetan Plateau. *Minerals* **2023**, *13*, 1390. <https://doi.org/10.3390/min13111390>

Academic Editor: Jaroslav Dostal

Received: 14 September 2023

Revised: 25 October 2023

Accepted: 29 October 2023

Published: 30 October 2023



**Copyright:** © 2023 by the authors. Licensee MDPI, Basel, Switzerland. This article is an open access article distributed under the terms and conditions of the Creative Commons Attribution (CC BY) license (<https://creativecommons.org/licenses/by/4.0/>).

## 1. Introduction

Highly fractionated or evolved granites are generally considered to be the ultimate products of extreme differentiation of a parent magma [1,2], and their origin has always been a focus of research on orogenic evolution [1,3]. Generally, these granites have a low content of mafic minerals, but are sometimes accompanied by intense rare-metal mineralization [1,4]. In terms of geochemistry, most highly fractionated granites are high-silica ( $\text{SiO}_2 > 75$  wt.%) and strongly peraluminous [5]. They are enriched in strong incompatible trace elements and significantly depleted in Ti, Eu, P, Sr, and Ba [6,7], and occasionally demonstrate relatively low Nb/Ta and Zr/Hf ratios [8,9]. It is noteworthy that the highly fractionated granites often exhibit significantly negative Eu anomalies and an REE tetrad effect [10], which is widely and controversially interpreted because of melt–fluid interaction [11,12], fluoride–silicate liquid immiscibility [13,14], or mineral fractionation [15,16]. These highly fractionated granites are extensively developed in regions such as the Hi-

malayan orogen and South China and can provide significant constraints on the magmatic processes and petrogenesis and geodynamic mechanisms.

In southeastern Tibet, the voluminous Eocene–Oligocene magmatism documents the post-collisional processes of the Indo–Asia interaction and provides direct magmatic records of the mantle melting and crustal evolution [17–20]. It has been recognized that the Eocene–Oligocene magmatism is dominated by potassic–ultrapotassic rocks, including adakite-like granites, quartz monzonites, shoshonitic syenites, lamprophyres, and basalts [18,21–26]. Some of the felsic intrusions host significant Cu(–Mo–Au) mineralization and form the Jinshajiang–Red River porphyry Cu-polymetallic metallogenic belt [21,23,24]. Recently, a suite of Eocene highly fractionated granite porphyries with high-silica and an REE tetrad effect was identified in Shiguanshan, western Yunnan. These non-adakitic Shiguanshan granite porphyries are significantly distinguished from the regional adakite-like granites but show a close spatial relationship with coeval mafic rocks and shoshonitic syenites, suggesting a possibly genetic relationship with the latter. To date, studies of Eocene–Oligocene magmatism have focused on potassic–ultrapotassic rocks and little or no information about highly fractionated granite porphyries is available. Thus, the process by which Eocene highly fractionated granite porphyries occur remains enigmatic, inhibiting detailed insight into the petrogenesis and geodynamic implications of those rocks, as well as the cause and mechanism of the REE tetrad effect in them.

This study reports the petrogenesis and tectonic setting of highly fractionated granite porphyries from the Shiguanshan, in western Yunnan, and the formation mechanism of the REE tetrad effect in them through analysis of zircon U–Pb age, mineral chemistry and Hf isotopic data, whole-rock elemental and Nd isotopic data, and fractionation modeling. Based on the comparison of whole-rock geochemistry between the Shiguanshan highly fractionated granite porphyries and the coeval mantle-derived shoshonitic rocks in adjacent regions, as well as modeling results using partition coefficients, we propose that the highly fractionated granite porphyries in the Shiguanshan area are A-type granites resulting from high-degree differentiation of the coeval syenite porphyries. Their formation is possibly related to lithospheric removal following the Indo–Asia collision. The occurrence of the REE tetrad effect in these highly fractionated samples can be attributed to mineral fractionation. Thus, our work provides significant insights into the origin and evolution of the Eocene highly fractionated granite porphyries and associated geodynamics in post-collisional settings of the SE Tibetan plateau.

## 2. Geological Setting and Petrography

The Tibetan Plateau, one of the typical representatives of continent–continent collision orogenic zone on the planet [27], consists of intricate tectonic collages involving some Paleozoic arc terranes, Gondwana-derived microcontinental fragments, and flysch complexes (Figure 1a) [28–30]. Tectonically, the SE Tibetan Plateau comprises principally the Simao–Indochina block, Songpan–Garzê fold belt, Baoshan and Tengchong blocks, and Yangtze Craton, which are separated by the Longmu Tso–Shuanghu, Changning–Menglian, Jinshajiang, and Ailaoshan–Song Ma suture zones (Figure 1a,b) [30,31].

The Yangtze Craton (SE Tibetan Plateau; Figure 1a,b) was positioned on the margin of Rodinia during the Neoproterozoic [32,33] and underwent two major geodynamic transitions from convergent plate settings related to arc subduction in the Early Neoproterozoic (Qingbaikouan) [34,35] to divergent plate settings related to a supercontinent breakup in the Middle–Late Neoproterozoic (Nanhua–Sinian) [36]. It contains a pre-Neoproterozoic crystalline basement covered by Late Neoproterozoic to Cenozoic sedimentary sequences [37,38]. There exist numerous remains of Neoproterozoic (1000–740 Ma) magmatic rocks with arc-like geochemical affinity within the western and northern margins of the craton. They are deemed to represent a Neoproterozoic continental arc developed at ca. 840 Ma, associated with the Panxi–Hannan arc [34], and discordantly covered by Late Neoproterozoic to Cretaceous strata [38]. The cover strata consist primarily of the Late Paleozoic to Early Mesozoic clastic–carbonate sequences and the Emeishan continental flood

basalts (260–250 Ma) associated with the Emeishan mantle plume [39,40]. During the Late Permian–Triassic, the closure of the Jinshajiang–Ailaoshan Ocean (a branch of the Paleo-Tethys) resulted in the formation of the Jinshajiang–Ailaoshan suture and Simao–Indochina block [41,42].

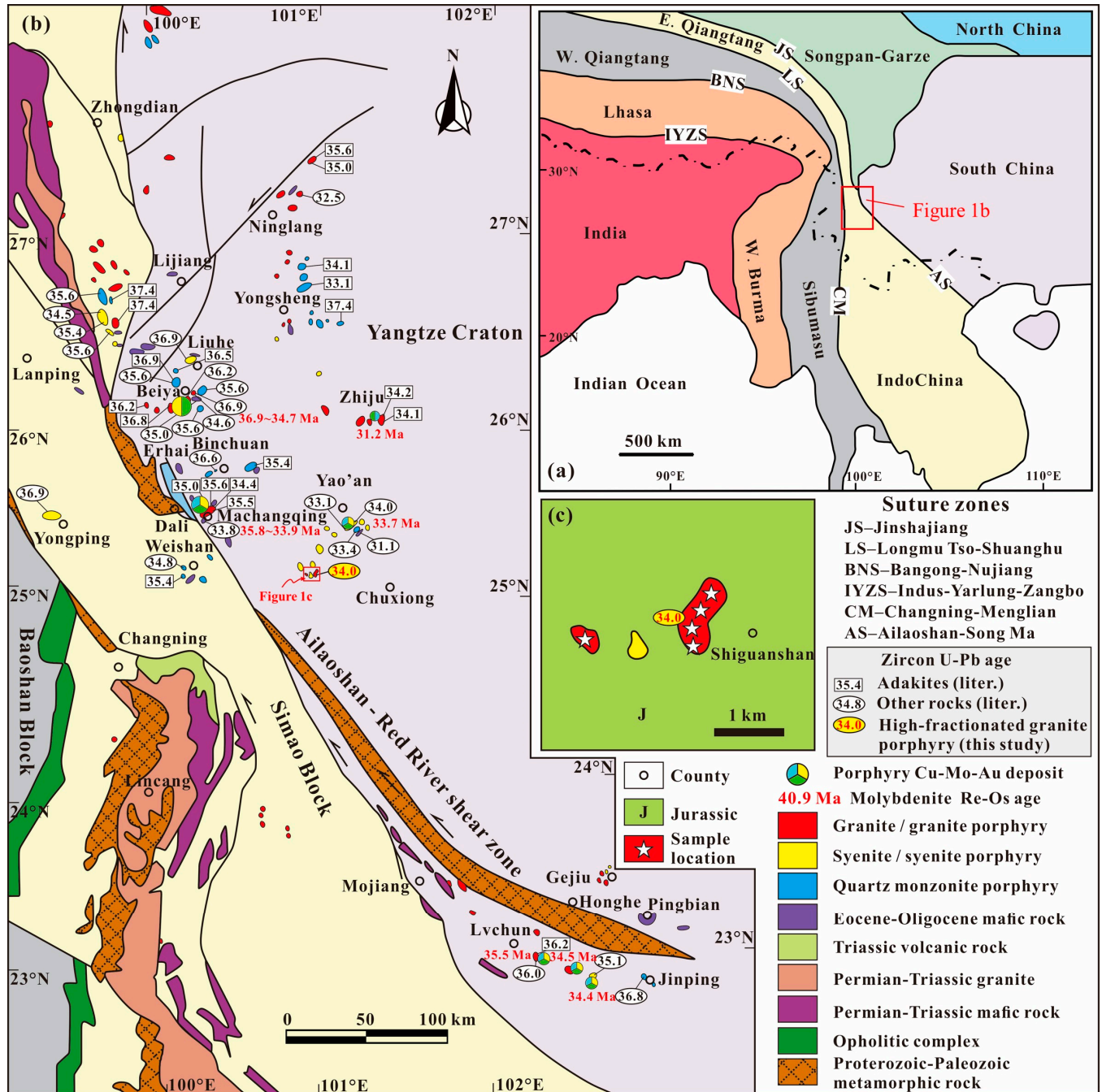


**Figure 1.** (a) Distribution of principal continental blocks and suture zones of Tibetan Plateau (modified from Metcalfe [31]). (b) Geological framework of western Yunnan in SE Tibetan Plateau showing the major Cenozoic magmatic rocks and porphyry Cu–Au–Mo deposits (modified from Lu et al. [19]; Deng et al. [30]). (c) Geological sketch map of the Shiguanshan granite porphyries, showing the locations of the studied samples.

The Indo–Asia collision resulted in significant potassic magmatism (ca. 43–32 Ma) in the western Yangtze Craton, proximal to the translithospheric Jinshajiang–Ailaoshan suture. These Eocene–Oligocene magmas, accordingly, form a long potassic igneous belt

in excess of 2000 km along the suture [25,43]; it includes both mafic and felsic lithologies (Figure 1b). The former is dominated by lamprophyre dykes [20,25] with a few potassic lavas [26], whereas the latter forms small-volume intrusions [22,44] comprising granite, syenite, and quartz monzonite in lithology, some of which host significant Cu(-Mo-Au) mineralization (Figure 1b).

The Shiguanshan highly fractionated granite porphyry is an Eocene high-silica magma suite in western Yunnan and is located in the southern part of the Jinshajiang–Ailaoshan potassic magmatic belt (Figure 1b). It also exhibits a close spatial relationship with the coeval Yao’an syenitic pluton (Figure 1b). These intrusive rocks occur within Jurassic mudstones (Figures 1c and 2a). The greyish–white granite porphyries are characterized by a porphyritic texture and contain phenocrysts of quartz (30–45 vol%), K-feldspar (55–65 vol%), and minor muscovite (1–10 vol%), which account for 35–40 vol% of the whole-rock (Figure 2b–f). Accessory minerals comprise zircon, titanite, monazite, allanite, and minimal apatite.

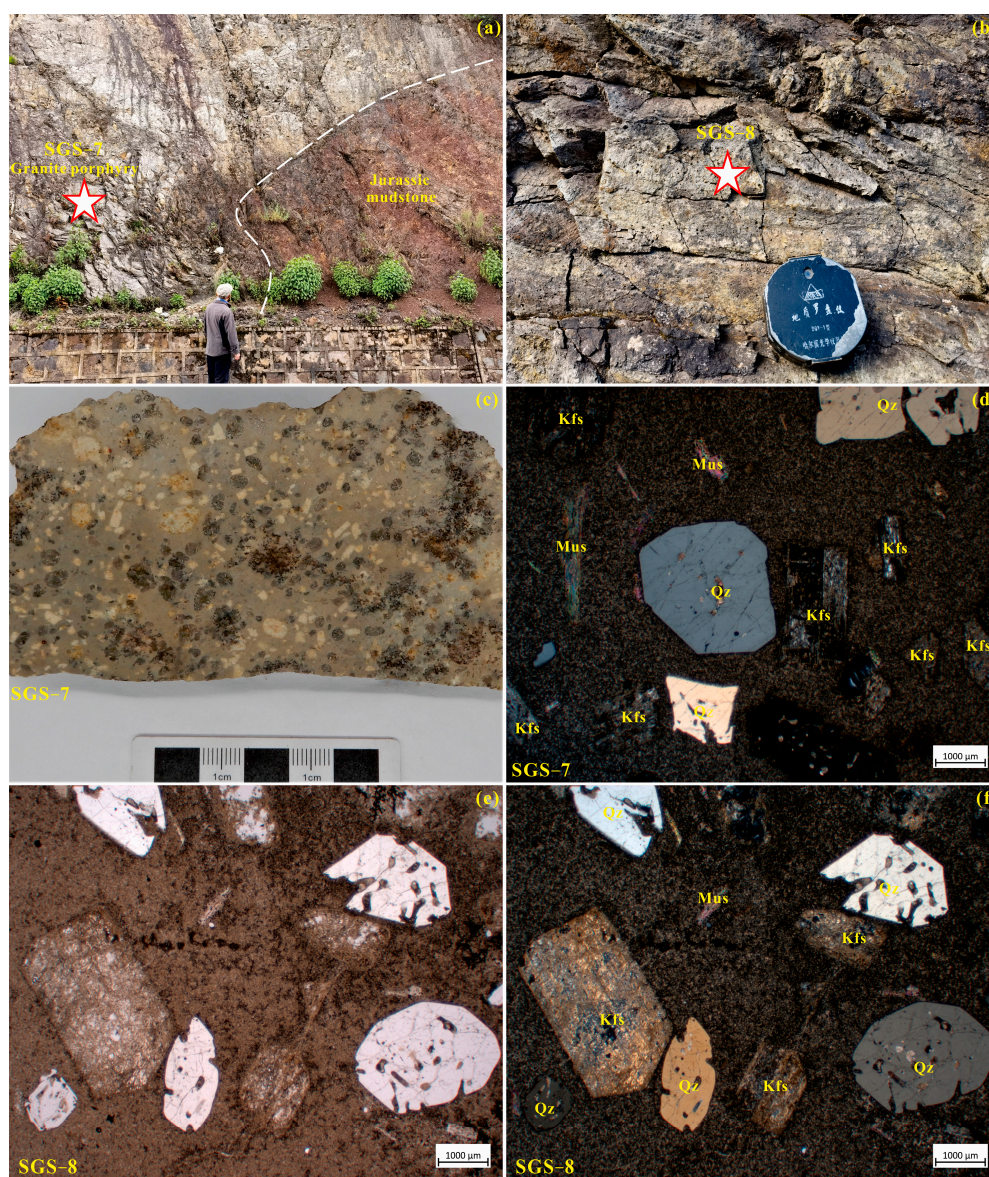


**Figure 2.** Field photographs and photomicrographs showing textural features and mineral assemblage of the Shiguanshan granite porphyries. Abbreviations: Kfs = K-feldspar, Qz = quartz, Mus = muscovite.

### 3. Analytical Methods

Zircon in situ U–Pb dating, trace element analysis, and Lu–Hf isotope, as well as whole-rock Sr–Nd isotopic compositions, were measured at the Wuhan SampleSolution Analytical Technology Co., Ltd., Wuhan, China. Whole-rock elemental analyses were carried out at the Northwest Geological Testing Center, a laboratory of the China Nonferrous Metal Mining Group Co., Ltd., Xian, China.

#### 3.1. Zircon U–Pb Dating and Trace Element Analysis

The procedure for zircon separation in sample processing included crushing, standard density and subsequent magnetic separation, and purification by handpicking. To reveal the internal zonation and inclusions, microphotographs of transmitted and reflected light, as well as cathodoluminescence (CL) images, were utilized. Different areas within the zircon grains were chosen for analysis based on their structures.

The U–Pb age and trace element were measured using an Agilent 7900 ICP-MS instrument (Agilent Technologies, Santa Clara, CA, USA) that was furnished with a 193 nm laser. The spot size and frequency of the laser were set to 32  $\mu\text{m}$  and 5 Hz, respectively. For data calibration, external standards such as Zircon Tanz and glass NIST610 were employed [45], respectively. The laser ablation system, the ICP-MS instrument, and the procedure for data reduction were carried out following the detailed operating conditions described by Zong et al. [46]. ICPMSDataCal [47] was used for data reduction and ISOPLOT (ver 3.0) [48] was used for age calculation and concordia diagrams.

#### 3.2. Zircon In Situ Lu–Hf Isotope Analyses

Experiments of in situ Hf isotope ratio analysis were conducted on the dated spots using a Neptune Plus MC-ICP-MS (Thermo Fisher Scientific, Bremen, Germany) in combination with a Geolas HD excimer ArF laser ablation system (Coherent, Göttingen, Germany). During analyses, a spot size of 44  $\mu\text{m}$  and laser repetition of 8 Hz with an energy density of  $\sim 7.0 \text{ J}/\text{cm}^2$  were used. Detailed operating conditions and the analytical method are the same as described by Hu et al. [49].

#### 3.3. Whole-Rock Major and Trace Elements

Representative samples were selected and powdered in an agate mill to a grain size of less than 200 mesh. The Rigaku Primus II X-ray fluorescence (XRF) system was employed to analyze the major elements of the whole-rock sample. The XRF analyses revealed that both the duplicate analyses and rock standards analyses of the samples exhibited relative standard deviations below 1%. REEs and trace element contents were measured by X-7 ICP-MS, with an analytical precision of  $\geq 10\%$ . Detailed analytical programs were described by Qi et al. [50].

#### 3.4. Whole-Rock Sr–Nd Isotopes

The Sr and Nd elements were extracted using a cation-exchange technique and their isotope ratios were measured using a Neptune Plus MC-ICP-MS (Thermo Fisher Scientific, Dreieich, Germany). An aliquot of the international standard solution containing  $200 \mu\text{g L}^{-1}$  was used for mass discrimination correction via internal normalization, resulting in an  $^{88}\text{Sr}/^{86}\text{Sr}$  ratio of 8.375209 and a  $^{146}\text{Nd}/^{144}\text{Nd}$  ratio of 0.7219 [51]. During the testing process, one international NIST 987 standard [52] was measured for every seven unknown samples analyzed. The analysis of the  $^{87}\text{Sr}/^{86}\text{Sr}$  ratio in the NIST 987 standard solution resulted in a measurement of  $0.710244 \pm 8$  (2SD,  $n = 5$ ), which is consistent with published values ( $0.710248 \pm 12$ ) [52] within the range of experimental error. One GSB 04-3258-2015 standard was measured for every seven samples analyzed. The analysis of the  $^{143}\text{Nd}/^{144}\text{Nd}$  ratio in the GSB 04-3258-2015 standard solution resulted in a measurement of  $0.512440 \pm 6$  (2SD,  $n = 9$ ), which is consistent with published values ( $0.512438 \pm 6$ ) [53] within the range of experimental error.

## 4. Results

### 4.1. Zircon U–Pb Geochronology and Trace Elements

The U–Pb dating and trace element analysis results are presented in Supplementary Tables S1 and S2, respectively, and illustrated through CL images, concordia diagrams, and normalized REE patterns (Figure 3). Zircon grains from the Shiguanshan highly fractionated granite porphyry are elongated, columnar, euhedral grains, with a length of 100–250  $\mu\text{m}$  (Figure 3a). In general, these zircons are transparent, and display clearly oscillatory zoning, without inherited cores under CL images (Figure 3a). The zircons have 2.6–20.2 ppm Pb, 253–2944 ppm Th, 378–2713 ppm U, and Th/U = 0.7–1.5 (Supplementary Table S1). They also display enrichment in HREEs, with marked positive Ce anomalies (108–316) and negative Eu anomalies (0.36–0.63) (Supplementary Table S2; Figure 3b). All these characteristics suggest that the zircons have a typical magmatic origin [54]. The  $^{206}\text{Pb}/^{238}\text{U}$  ages of 22 zircon grains from sample SGS-7 are 33.1–35.1 Ma, with a weighted average of  $34.0 \pm 0.3$  Ma (MSWD = 2.8) (Figure 3a).

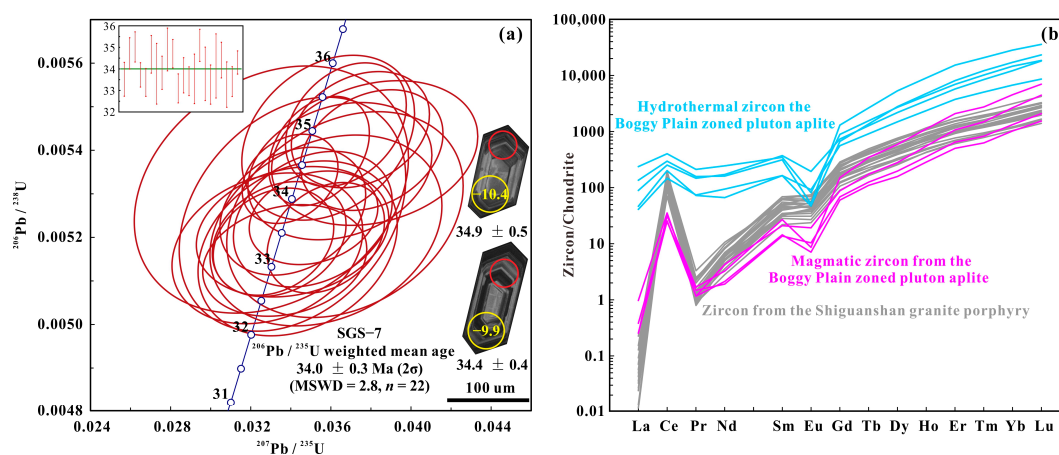


**Figure 3.** (a) Zircon U–Pb concordia diagrams and CL images for representative zircon grains from the Shiguanshan highly fractionated granite porphyry, with red and yellow circles showing areas of U–Pb and Lu–Hf isotope analysis, respectively. (b) Chondrite-normalized REE patterns of zircons from the Shiguanshan highly fractionated granite porphyry and of typical magmatic and hydrothermal zircons [55]. Chondrite data are from Sun and McDonough [56].

### 4.2. Geochemical and Isotopic Results

#### 4.2.1. Major and Trace Elements

The whole-rock elemental composition for the Shiguanshan granite porphyry and coeval Yao’an syenite porphyry are compiled from the published literature and this study (Supplementary Table S3). All the Shiguanshan samples fall within the subalkaline granite field in a total alkali–silica (TAS) diagram (Figure 4a), with high  $\text{SiO}_2$  (78.16–79.13 wt.%) content. They show high  $\text{K}_2\text{O}$  (3.99–4.90 wt.%) and low  $\text{CaO}$  (0.17–0.27 wt.%) and are high-K calc-alkalic rocks (Figure 4b). All samples are strongly peraluminous (Figure 4c), with A/CNK (molar  $\text{Al}_2\text{O}_3/(\text{CaO} + \text{Na}_2\text{O} + \text{K}_2\text{O})$ ) = 1.95–2.80 (Supplementary Table S3). They have a high differentiation index ( $\text{DI} = 87.2\text{--}90.0$ ; from CIPW calculating values) and low  $\text{MgO}$  (0.21–0.26 wt.%) content and belong to highly fractionated granite (Figure 4d). Most major elements of Shiguanshan granite porphyries and coeval Yao’an syenite porphyries exhibit a linear association with  $\text{SiO}_2$  (Supplementary Table S3). For example,  $\text{TiO}_2$ ,  $\text{Al}_2\text{O}_3$ , and  $^{\text{T}}\text{Fe}_2\text{O}_3$  show inverse correlation trends with  $\text{SiO}_2$  (Figure 5a–c). This suggests that these intrusions should be genetically connected, perhaps by fractional crystallization.

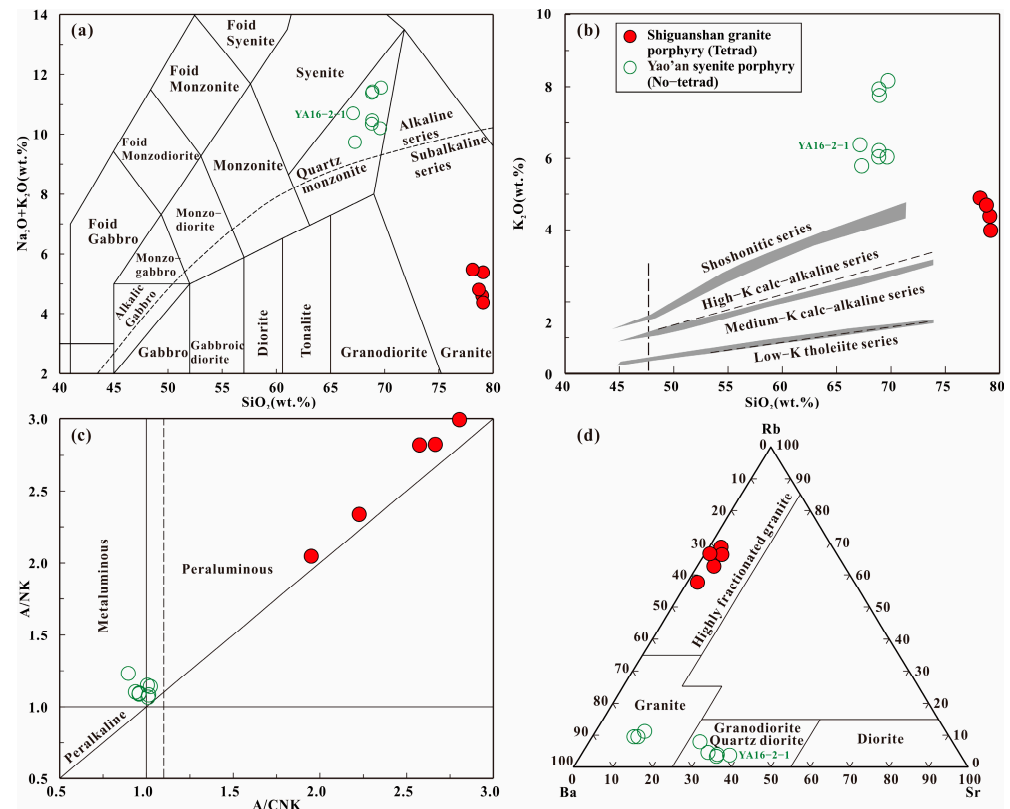


**Figure 4.** Classification diagrams of (a)  $(K_2O + Na_2O)$  vs.  $SiO_2$  [57], (b)  $K_2O$  vs.  $SiO_2$  [58], (c)  $A/NK$  vs.  $A/CNK$  [59], and (d)  $Rb$ – $Ba$ – $Sr$  [60]. The coeval Yao’an syenite porphyries are from Luo et al. [61] and are given in Supplementary Table S3.

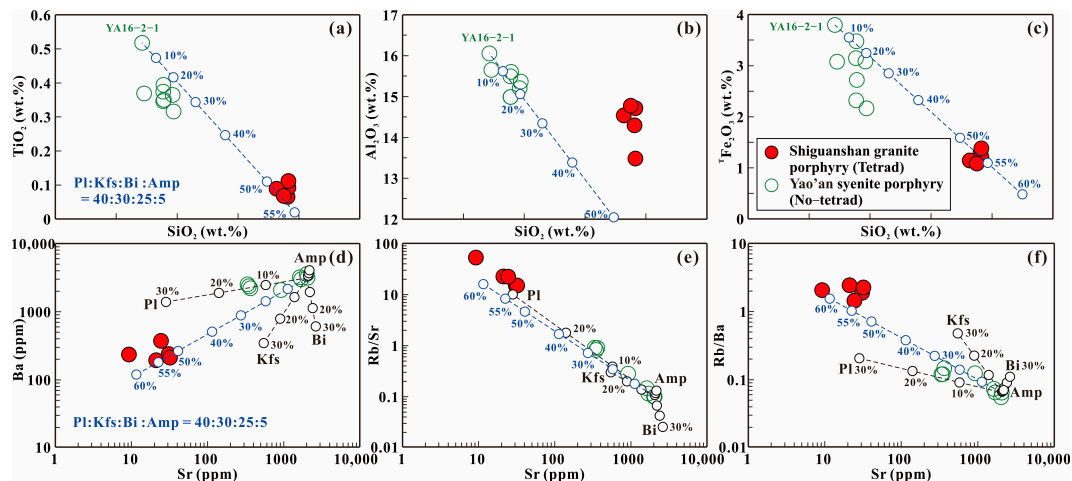


**Figure 5.** Diagrams for fractionation modeling of (a)  $TiO_2$  vs.  $SiO_2$ , (b)  $Al_2O_3$  vs.  $SiO_2$ , (c)  $TFe_2O_3$  vs.  $SiO_2$ , (d)  $Ba$  vs.  $Sr$ , (e)  $Rb/Sr$  vs.  $Sr$ , and (f)  $Rb/Ba$  vs.  $Sr$ . Sample YA16-2-1, with the lowest  $SiO_2$  from the coeval Yao’an syenite porphyries [61], is assumed to represent the parental magma composition. The mineral compositions of fractionated minerals are from Xu and Qiu [62] and are given in Supplementary Table S4a. The partition coefficients of trace elements are from Nash and Crecraft [63] and Tiepolo et al. [64]. The partitioning coefficients, fractionated mineral assemblage, and modeling results are listed in Supplementary Table S4b,c. Data sources are the same as in Figure 4.

Similarly, to the Yao’an syenite porphyries, the Shiguanshan granite porphyries exhibit obvious enrichment of light REEs (LREEs) with  $(La/Yb)_N$  of 1.82–7.80, but with more significant Eu negative anomalies with  $Eu/Eu^*$  of 0.50–0.80 (Figure 6a). Both the felsic

intrusions from Shiguanshan and Yao’an exhibit enrichment in Pb, U, Th, and Rb, as well as depletion in Ti, Eu, P, Sr, and Ba. These enrichments and depletions are particularly pronounced in the granitic rocks (Figure 6b). They both exhibit non-adakite-like affinities, with low Sr/Y ratios (0.35–106.89) and high Y/Ho ratios (25.69–42.43) (Supplementary Table S3). It should be noted that the Shiguanshan granite porphyries exhibit an obvious REE tetrad effect, with TE<sub>1,3</sub> of 0.98–1.21, average 1.11 (Supplementary Table S3) [10]. In addition, the tetrad granite porphyries have lower LREEs compared with the No-tetrad syenite porphyries. The (La/Yb)<sub>N</sub>, La/La\*, and Nd/Nd\* ratios show inverse correlation trends with TE<sub>1,3</sub> values from the syenite porphyries to granite porphyries (Figure 7).

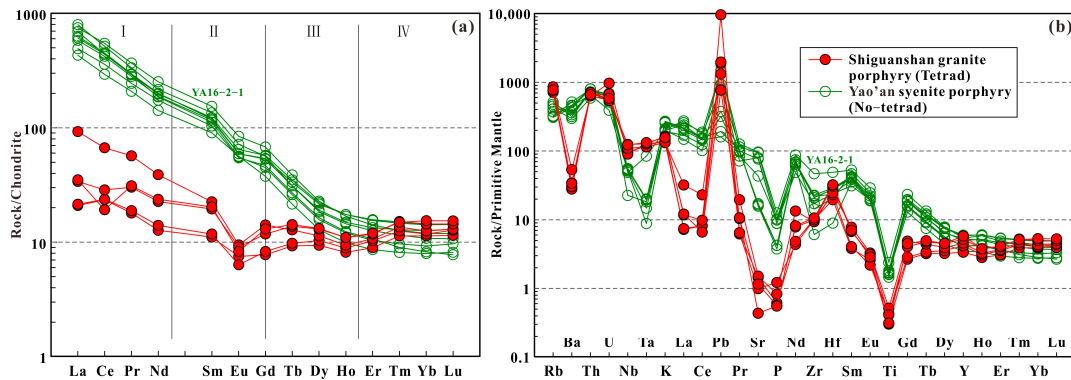


**Figure 6.** (a) Chondrite-normalized REE and (b) primitive-mantle-normalized trace element patterns for the Shiguanshan granite porphyries and coeval Yao’an syenite porphyries. Values for normalization are from Sun and McDonough [56]. Data sources are the same as in Figure 4.

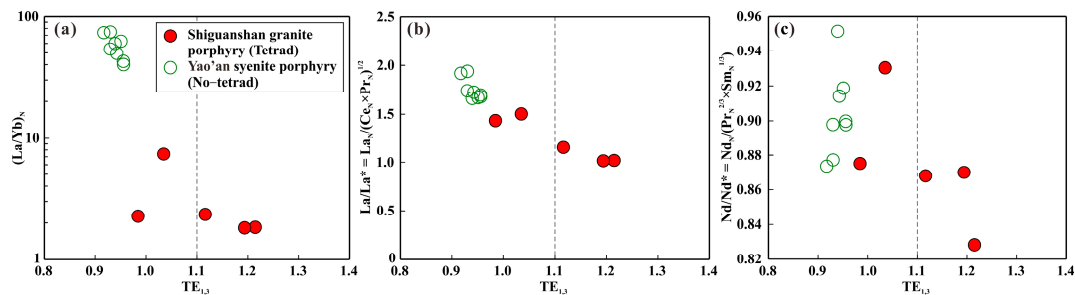


**Figure 7.** (a) (La/Yb)<sub>N</sub> vs. TE<sub>1,3</sub> plots; (b) La/La\* vs. TE<sub>1,3</sub> plots; and (c) Nd/Nd\* vs. TE<sub>1,3</sub> plots. TE<sub>1,3</sub> = [(Ce/Ce\* × Pr/Pr\*)<sup>0.5</sup> × (Tb/Tb\* × Dy/Dy\*)<sup>0.5</sup>] [10]. Data sources are the same as in Figure 4.

#### 4.2.2. Sr–Nd Isotopes

The whole-rock Sr–Nd isotopic compositions for the Shiguanshan granite porphyries are listed in Table 1 and illustrated in Figure 8a. Due to the high Rb/Sr ratios (14.89–53.45; Supplementary Table S3) commonly observed in granitic samples, the radiogenic <sup>86</sup>Sr content is also high, leading to significant errors and a wide range of calculated (<sup>87</sup>Sr/<sup>86</sup>Sr)<sub>i</sub> ratios (0.70470–0.70837). As a result, the reliability of Sr isotope data from these samples are relatively poor. However, the variation range of Sm/Nd ratios (0.19–0.29; Supplementary Table S3) is relatively limited, and thus the Nd isotope data are relatively stable. In this context, two granitic samples exhibit negative ε<sub>Nd</sub>(t) values (−12.8 to −12.3; Figure 8a) and uniform two-stage Nd-isotope depleted mantle model ages (T<sub>DM2</sub> = 1.8 Ga) (Table 1).

#### 4.2.3. Zircon Lu–Hf Isotopes

In situ Lu–Hf isotopic analyses of all zircons were performed on the same grains that were used for U–Pb ages. The zircon Lu–Hf isotopic data and calculation method are provided in Table 2 for the Shiguanshan granite porphyry and illustrated in Figure 8b. Zircon spot analyses from the granite porphyry (SGS-7, 12 spots) show <sup>176</sup>Hf/<sup>177</sup>Hf ratios

ranging from 0.282456 to 0.282502, with negative  $\epsilon_{\text{Hf}}(t)$  values ranging from  $-10.4$  to  $-8.8$ . The two-stage Hf mantle model ages ( $T_{\text{DM}2}$ ) range from 1.8 to 1.7 Ga.

**Table 1.** Whole-rock Sr–Nd isotopic data for the Shiguanshan granite porphyry in western Yunnan.

Sample	$^{87}\text{Rb}/^{86}\text{Sr}$	$^{87}\text{Sr}/^{86}\text{Sr}$	$2\sigma$	$(^{87}\text{Sr}/^{86}\text{Sr})_i$	$^{147}\text{Sm}/^{144}\text{Nd}$	$^{143}\text{Nd}/^{144}\text{Nd}$	$2\sigma$	$(^{143}\text{Nd}/^{144}\text{Nd})_i$	$\epsilon_{\text{Nd}}(t)$	$T_{\text{DM}2}$ (Ma)
SGS-7	43.902	0.729566	0.000007	0.70837	0.1150	0.511963	0.000007	0.511937	$-12.82$	1887
SGS-8	64.9084	0.736048	0.000005	0.70470	0.1707	0.512004	0.000007	0.511966	$-12.26$	1829

Notes:  $^{87}\text{Rb}/^{86}\text{Sr}$  and  $^{147}\text{Sm}/^{144}\text{Nd}$  are calculated using whole-rock Rb, Sr, Sm, and Nd values in Supplementary Table S3;  $(^{87}\text{Sr}/^{86}\text{Sr})_i = (^{87}\text{Sr}/^{86}\text{Sr})_s - (^{87}\text{Rb}/^{86}\text{Sr}) \times (e^{\lambda t} - 1)$ ;  $\lambda_{\text{Rb-Sr}} = 1.42 \times 10^{-11} \text{ year}^{-1}$ ;  $^{87}\text{Rb}/^{86}\text{Sr} = (\text{Rb}/\text{Sr}) \times 2.8956$ ;  $\epsilon_{\text{Nd}}(t) = [(^{143}\text{Nd}/^{144}\text{Nd})_i / (^{143}\text{Nd}/^{144}\text{Nd})_{\text{CHUR}}(t) - 1] \times 10,000$ ;  $(^{143}\text{Nd}/^{144}\text{Nd})_i = (^{143}\text{Nd}/^{144}\text{Nd})_s - (^{147}\text{Sm}/^{144}\text{Nd}) \times (e^{\lambda t} - 1)$ ;  $(^{143}\text{Nd}/^{144}\text{Nd})_{\text{CHUR}}(t) = 0.512638 - 0.1967 \times (e^{\lambda t} - 1)$ ;  $\lambda_{\text{Sm-Nd}} = 6.54 \times 10^{-12} \text{ year}^{-1}$ ;  $^{147}\text{Sm}/^{144}\text{Nd} = (\text{Sm}/\text{Nd}) \times 0.60456$ ;  $T_{\text{DM}} = 1/\lambda_{\text{Sm-Nd}} \times \ln \{1 + [(^{143}\text{Nd}/^{144}\text{Nd})_s - 0.51315] / [(^{147}\text{Sm}/^{144}\text{Nd})_s - 0.2137]\}$ , where subscripts S, CHUR, and DM represent the sample, Chondritic Uniform Reservoir, and depleted mantle, respectively. Chondritic Uniform Reservoir (CHUR) at the present day  $[(^{147}\text{Sm}/^{144}\text{Nd})_{\text{CHUR}} = 0.1967$ ;  $(^{143}\text{Nd}/^{144}\text{Nd})_{\text{CHUR}} = 0.512638]$  [65,66] was used for the calculations. Nd depleted mantle model ages ( $T_{\text{DM}}$ ) were calculated using  $(^{147}\text{Sm}/^{144}\text{Nd})_{\text{DM}} = 0.2137$  and  $(^{143}\text{Nd}/^{144}\text{Nd})_{\text{DM}} = 0.51315$  [67] at the present day.  $\lambda_{\text{Rb}} = 1.42 \times 10^{-11} \text{ year}^{-1}$  [68];  $\lambda_{\text{Sm}} = 6.54 \times 10^{-12} \text{ year}^{-1}$  [69]. Initial  $^{87}\text{Sr}/^{86}\text{Sr}$  ratios and  $\epsilon_{\text{Nd}}(t)$  values are corrected at the ages based on the zircon U–Pb dating.

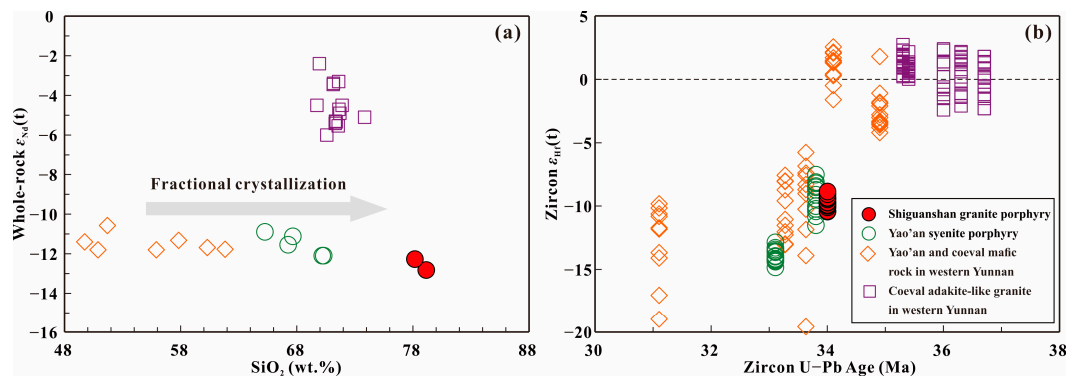


**Figure 8.** Plots of (a)  $\text{SiO}_2$  vs. whole-rock  $\epsilon_{\text{Nd}}(t)$  values and (b) zircon U–Pb ages vs.  $\epsilon_{\text{Hf}}(t)$  values for the Cenozoic felsic and mafic rocks in western Yunnan. Data are from Lu et al. [20], Shen et al. [22], Chang et al. [24], Guo et al. [25], Luo et al. [61], He et al. [70], Yan et al. [71,72], and Yang et al. unpublished.

**Table 2.** Hf isotopic compositions for zircon from the Shiguanshan highly fractionated granite porphyry (SGS-7) in western Yunnan.

Spot	$^{176}\text{Yb}/^{177}\text{Hf}$	$^{176}\text{Lu}/^{177}\text{Hf}$	$^{176}\text{Hf}/^{177}\text{Hf}$	$1\sigma$	$^{176}\text{Hf}/^{177}\text{Hf}_i$	$\epsilon_{\text{Hf}}(0)$	$\epsilon_{\text{Hf}}(t)$	$T_{\text{DM}1}$ (Ma)	$T_{\text{DM}2}$ (Ma)	$f_{\text{Lu}/\text{Hf}}$
1	0.033915	0.001009	0.282477	0.000015	0.282476	$-10.4$	$-9.7$	1095	1729	$-0.97$
2	0.046189	0.001395	0.282470	0.000017	0.282469	$-10.7$	$-10.0$	1116	1745	$-0.96$
3	0.028756	0.000891	0.282483	0.000012	0.282483	$-10.2$	$-9.5$	1083	1715	$-0.97$
4	0.041486	0.001294	0.282456	0.000017	0.282456	$-11.2$	$-10.4$	1132	1775	$-0.96$
5	0.038821	0.001179	0.282458	0.000012	0.282457	$-11.1$	$-10.4$	1127	1773	$-0.96$
6	0.046810	0.001398	0.282502	0.000013	0.282501	$-9.6$	$-8.8$	1071	1674	$-0.96$
7	0.035780	0.001057	0.282467	0.000012	0.282466	$-10.8$	$-10.1$	1111	1753	$-0.97$
8	0.022749	0.000704	0.282487	0.000013	0.282487	$-10.1$	$-9.3$	1072	1706	$-0.98$
9	0.030921	0.000919	0.282472	0.000012	0.282471	$-10.6$	$-9.9$	1100	1741	$-0.97$
10	0.034426	0.001041	0.282487	0.000014	0.282486	$-10.1$	$-9.4$	1082	1707	$-0.97$
11	0.042083	0.001310	0.282478	0.000013	0.282477	$-10.4$	$-9.7$	1102	1727	$-0.96$
12	0.046712	0.001464	0.282496	0.000016	0.282495	$-9.8$	$-9.1$	1081	1687	$-0.96$

Notes:  $\epsilon_{\text{Hf}}(t) = 10000 \times \{[(^{176}\text{Hf}/^{177}\text{Hf})_s - (^{176}\text{Lu}/^{177}\text{Hf})_s \times (e^{\lambda t} - 1)] / [(^{176}\text{Hf}/^{177}\text{Hf})_{\text{CHUR},0} - (^{176}\text{Lu}/^{177}\text{Hf})_{\text{CHUR}} \times (e^{\lambda t} - 1)] - 1\}$ ;  $T_{\text{DM}1} = 1/\lambda \times \ln \{1 + [(^{176}\text{Hf}/^{177}\text{Hf})_s - (^{176}\text{Hf}/^{177}\text{Hf})_{\text{DM}}] / [(^{176}\text{Lu}/^{177}\text{Hf})_s - (^{176}\text{Lu}/^{177}\text{Hf})_{\text{DM}}]\}$ ;  $T_{\text{DM}2} = 1/\lambda \times \ln \{1 + [(^{176}\text{Hf}/^{177}\text{Hf})_{s,t} - (^{176}\text{Hf}/^{177}\text{Hf})_{\text{DM},t}] / [(^{176}\text{Lu}/^{177}\text{Hf})_C - (^{176}\text{Lu}/^{177}\text{Hf})_{\text{DM}}] + t\}$ ;  $f_{\text{Lu}/\text{Hf}} = (^{176}\text{Lu}/^{177}\text{Hf})_s / (^{176}\text{Lu}/^{177}\text{Hf})_{\text{CHUR}} - 1$ ;  $(^{176}\text{Lu}/^{177}\text{Hf})_{\text{CHUR}} = 0.0332$  and  $(^{176}\text{Hf}/^{177}\text{Hf})_{\text{CHUR},0} = 0.282772$  [73];  $(^{176}\text{Lu}/^{177}\text{Hf})_{\text{DM}} = 0.0384$  and  $(^{176}\text{Hf}/^{177}\text{Hf})_{\text{DM}} = 0.28325$  [74];  $\lambda = 1.867 \times 10^{-11} \text{ year}^{-1}$  [75];  $(^{176}\text{Lu}/^{177}\text{Hf})_C = 0.015$  [76];  $t = 34 \text{ Ma}$ .

## 5. Discussion

### 5.1. Age of the Shiguanshan Granite Porphyry

Zircon grains from the Shiguanshan granite porphyry lack complex core-rim textures and exhibit concordant U–Pb ages (Figure 3a), indicating that their weighted mean  $^{206}\text{Pb}/^{238}\text{U}$  ages represent the timing of crystallization of the magma. In this study, we gain the crystallization age of Shiguanshan granite porphyry (SGS-7) at  $34.0 \pm 0.3$  Ma (Figure 3a), which coincides with those of syenite porphyry in the Yao'an area (ca. 33 Ma) [23,61]. In addition, the Shiguanshan granite porphyries are contemporaneous with the adjacent (e.g., Beiya and Machangqing) adakite-like granites and mafic rocks in western Yunnan, which were emplaced ranging from 37 to 31 Ma (Figure 1b).

### 5.2. Petrogenesis of the Shiguanshan Granite Porphyry

The Shiguanshan Tetrad granite porphyries and Yao'an No-tetrad syenite porphyries exhibit similar tectonic settings, whole-rock elemental (excluding REEs) and Nd isotopic compositions, and zircon Hf isotopic compositions, indicating a similar genetic type, comparable processes of fractional crystallization, and a shared magma source.

#### 5.2.1. Genetic Type: Highly Fractionated A-Type Granites

The Shiguanshan samples exhibit characteristics of peraluminous high-silica granites ( $\text{SiO}_2 > 75$  wt.%) [6], with high DI, low MgO content, enriched abundances of Pb, U, Th, and Rb, and depleted abundances of Ti, Eu, P, Sr, and Ba (Figures 4–6). These features align with those typically observed in highly fractionated granites (Figure 4d) [77]. Due to the similar mineral assemblage and geochemical compositions of high differentiation granites, it is difficult to distinguish their petrogenetic type [78]. Fortunately, the coeval low-silica Yao'an felsic rocks that are genetically associated with the Shiguanshan highly fractionated granite porphyries may preserve more original characteristics of the parent magma.

In the genetic type diagrams for granites, the Yao'an syenite porphyries fall within the A-type granite field (Figure 9). In addition, the sample (YA16-2-1) with the lowest  $\text{SiO}_2$  content ( $\text{SiO}_2 = 67.12$  wt.%) in the Yao'an syenite porphyries displays the highest zircon saturation temperature ( $883^\circ\text{C}$ ; Supplementary Table S3) [79], which may represent the initial temperature of the magma and possess characteristics of high-temperature magma [80]. These characteristics suggest that the Yao'an syenite porphyries exhibit an A-type granite affinity. For the Shiguanshan highly fractionated granite porphyries, the absence of zircon inheritance (Figure 3a) and relatively uniform zircon Hf isotopes (Figure 8b) exclude the possibility of it being S-type rocks. In the genetic classification diagram, the Shiguanshan granite porphyries and the coeval adakite-like granites in western Yunnan distinctly fall into different ranges (Figure 9), with the latter showing affinity to I-type granites. It is important that the Shiguanshan granite porphyries have high zircon saturation temperatures ( $803\text{--}829^\circ\text{C}$ , average  $819^\circ\text{C}$ ; Supplementary Table S3) and exhibit a trend of evolving from A-type granites towards fractionated granites (Figure 9e,f). Accordingly, the Shiguanshan granite porphyries can be classified as highly fractionated A-type granites, which possibly evolved from the adjacent and coeval Yao'an A-type granites. In addition, the Y/Nb ratios of these samples do not show significant changes during magma evolution, and they are all less than 1.2. Therefore, they can be further classified as  $A_1$ -type granites, as proposed by Eby [81] (Figure 10).

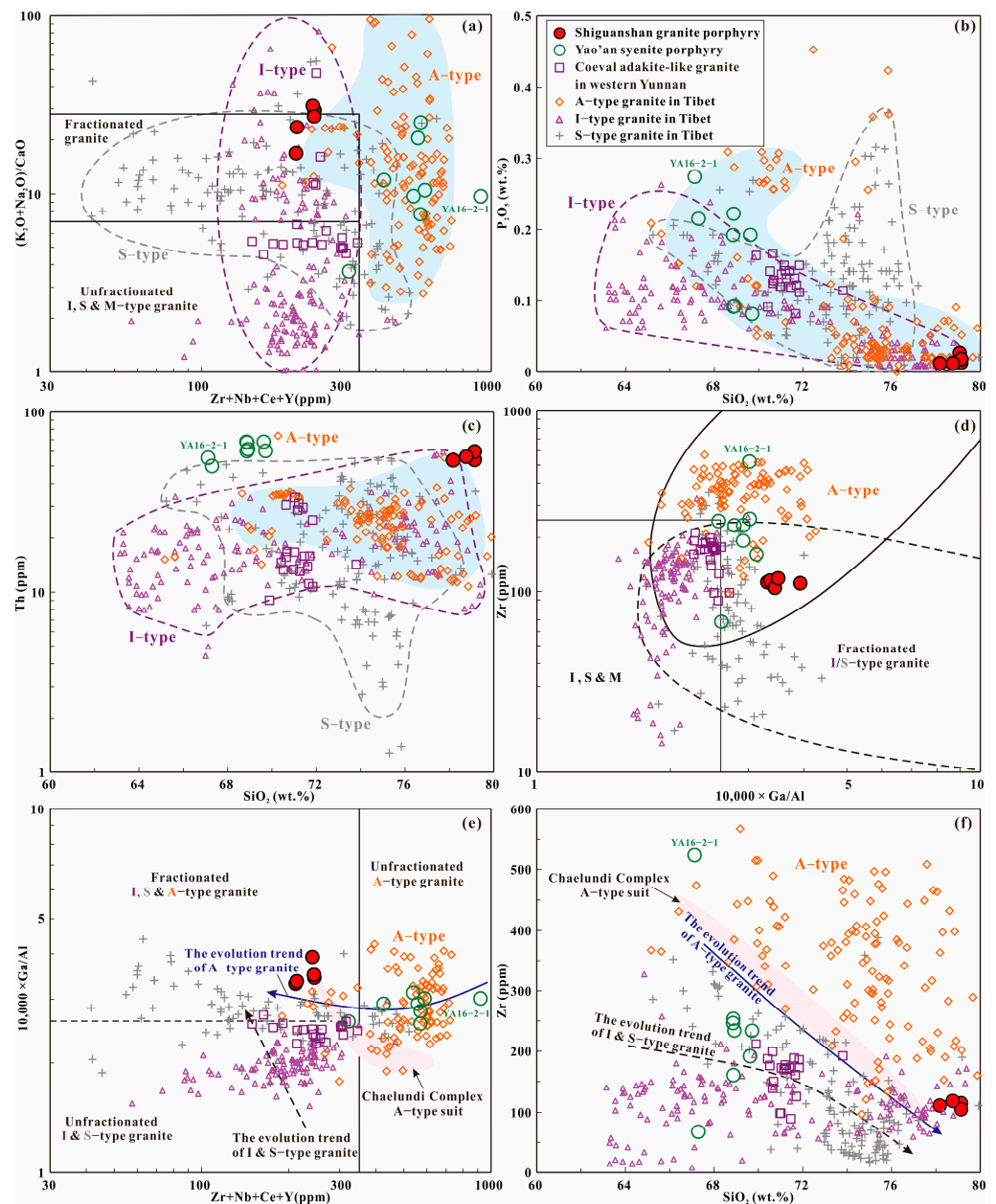


**Figure 9.** Genetic type diagrams for granitic rocks. (a)  $(K_2O + Na_2O)/CaO$  vs.  $Zr + Nb + Ce + Y$  plots [82]. (b)  $P_2O_5$  vs.  $SiO_2$  plots. (c) Th vs.  $SiO_2$  plots. (d) Zr vs.  $10,000 \times Ga/Al$  plots [5]. (e)  $10,000 \times Ga/Al$  vs.  $Zr + Nb + Ce + Y$  plots. (f) Zr vs.  $SiO_2$  plots. The data of the A-type, I-type, and S-type granitic rocks in Tibet are from Shuai et al. [83] and references therein. The data of the coeval adakite-like granites in western Yunnan are from He et al. [70] and Shen et al. [22]. The data of the Chaelundi Complex A-type suit are from Landenberger and Collins [84].

### 5.2.2. Fractional Crystallization Processes

Field investigation, mineral species, and their chemical variations, as well as geochemical compositions, support the occurrence of effective fractional crystallization in granite magmas [5]. On the Harker diagrams, most major elements of Shiguanshan granite porphyries and coeval Yao'an syenite porphyries display linear trends with  $SiO_2$ , implying features of differentiation. For example, the decreasing trend of  $Al_2O_3$ ,  $TFe_2O_3$ , and  $TiO_2$  indicates the fractionation of plagioclase, K-feldspar, biotite, amphibole, and Fe–Ti oxides (Figure 5a–c). The  $P_5O_2$  content (Figure 9b) is mainly controlled by apatite. The significant Eu negative anomalies supporting the plagioclase play a significant role as a

fractionating phase (Figure 6a). As discussed above, the high-level fractionation of the Yao'an syenite porphyries may result in the generation of high-silica granite porphyries in the Shiguanshan, which is in accordance with previous interpretations suggesting the evolution of intermediate-felsic magmas to the silicic extreme through ultimate high-level fractionation and melt extraction [85]. Quantitative modeling using mass balance reveals that the Shiguanshan granite porphyries likely formed through the fractional crystallization of a mineral assemblage consisting of plagioclase, K-feldspar, biotite, and amphibole (in a ratio of 40:30:25:5). This fractionation process is estimated to have a degree of 50%–55%. The assumption is made that the parental magma composition is represented by the lowest felsic sample YA16-2-1 from the coeval Yao'an syenite porphyries (Figure 5a–c), and the mineral assemblage is common in the Yao'an intrusion [23,61]. In this model, the deviation of  $Al_2O_3$  (Figure 5b) may be attributed to the presence of muscovite, which occurs in the late stages of acidic magma. This fractionation process is also confirmed by modeling results of trace elements (e.g., Rb, Sr, and Ba), which are mainly influenced by feldspar (Figure 5d–f). It is worth mentioning that the Shiguanshan granite porphyries could potentially undergo a higher degree of differentiation (>55%) due to the possibility of the parental magma having lower  $SiO_2$  content compared to the Yao'an syenite porphyries.

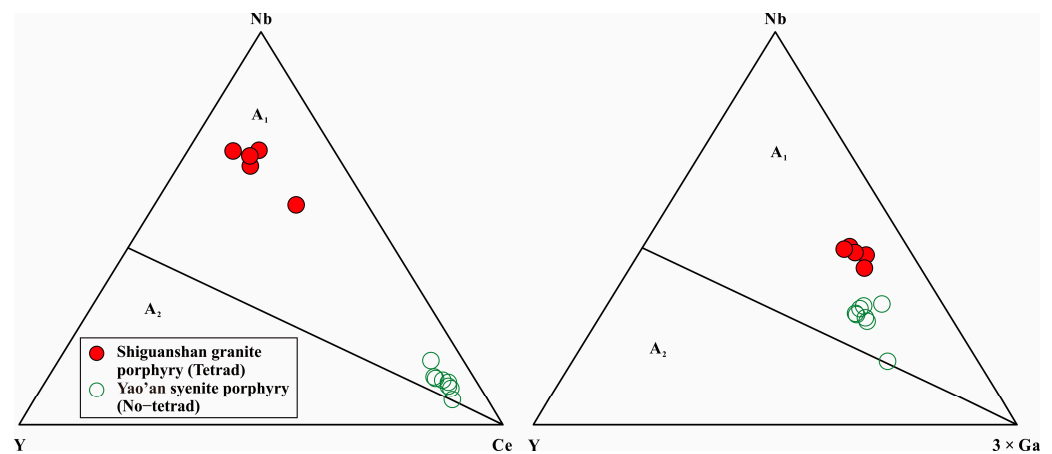


**Figure 10.** The  $A_1$  and  $A_2$  subgroup discriminations [81] of A-type granites for the Shiguanshan granite porphyries and coeval Yao'an syenite porphyries. Data sources are the same as in Figure 4.

### 5.2.3. Magma Source

The origin of A-type granites remains hotly debated, with proposed ideas involving the melting of crustal sources, crust- and mantle-derived magma mixing, or fractional crystallization, with/without crustal assimilation of mantle-derived magmas [81,86,87]. No mafic dykes and enclaves were observed within the Shiguanshan granite porphyries, together with the relatively uniform zircon Hf isotopes (Figure 8b), indicating a lack of magma mixing in the Shiguanshan granite porphyries. Additionally, they have different Nd–Hf isotopic compositions from the coeval adakite-like granites in western Yunnan (Figure 8), indicating that these intrusions were probably not derived from thickened mafic lower crust [22,70]. The high  $SiO_2$  (78.16–79.13 wt.%) and low MgO (0.21–0.26 wt.%) content of the Shiguanshan granite porphyries suggest that they were not directly derived from the upper mantle, as lithospheric mantle cannot generate melts with  $SiO_2$  concentrations higher than those of dacite ( $SiO_2 < 55$  wt.%) [88]. It is important to note that the large variation of zircon  $\varepsilon_{Hf}(t)$  values of the Shiguanshan granite porphyries and Yao'an syenite porphyries (Figure 8b) suggests enriched sources, e.g., sediments [89], continental crust, and/or enriched mantle components [90]. Furthermore, both the Shiguanshan granite porphyries and Yao'an syenite porphyries exhibit similar enriched Nd isotopic compositions to the coeval mafic rocks in western Yunnan (Figure 8b), indicating that they share a similar magma source, that is, enriched lithospheric mantle. This is consistent with the mantle-derived  $A_1$ -type granite Eby [81].

### 5.3. The Formation Mechanism of the REE Tetrad Effect in Shiguanshan Granite Porphyries

REEs generally behave similarly in purely magmatic systems and show smooth chondrite-normalized patterns, except for Ce and Eu. However, many highly fractionated granites exhibit abnormal REE patterns with the tetrad effect [91]. There are three controversial processes used to explain this formation mechanism: (1) The melt–fluid interaction during magmatic–hydrothermal transition [10,91,92]; (2) The fluoride–silicate liquid immiscibility in F-rich magmatic systems [13,14]; (3) The fractionation of accessory minerals during magmatic evolution or magmatic–hydrothermal transition [15,83,93].

Petrographic observations show that intrusions with a significant REE tetrad effect caused by melt–fluid interaction commonly undergo extensively hydrothermal alteration (e.g., albitization or greisenization) and generate hydrothermal minerals, such as fluorites and hydrothermal zircons [11,55]. However, the Shiguanshan granite porphyries exhibit pristine magmatic textures (Figure 2) and contain typical magmatic zircons (Figure 3). No observation of hydrothermal alteration minerals was made (Figure 2). These features indicate that hydrothermal fluid activity is insignificant in the Shiguanshan granite porphyries. In terms of geochemistry, some intrusions with a significant REE tetrad effect ( $TE_{1,3} > 1.1$ ) often exhibit decreased twin-elemental ratios (e.g., leucogranites from Ongon Khaikhan; Figure 11a–c) [9,11], which are different from their usual chondritic ratios ( $Nb/Ta = 17.6$ ,  $Zr/Hf = 36.3$ , and  $K/Rb = 235$ ) [56] in purely magmatic systems [94], suggesting fractionation of twin-elements within these rocks (Figure 11a–c). Researchers attribute this coupling between the twin-elemental fractionation and REE tetrad effect to melt–fluid interaction [10,11,91], whereas the ratios of twin-elements of both the No-tetrad Yao’an syenite porphyries and Shiguanshan Tetrad granite porphyries are broadly within the range of common granites (Figure 11a–c) and closely resemble chondritic ratios, indicating a decoupling between the REE tetrad effect and fractionation of twin-elements. Similar examples can be seen in other granites reported elsewhere, such as the Gaijin batholith [83] and Zengjialong granites [95] (Figure 11a–c). Moreover, peraluminous granites that demonstrate substantial indications of interaction with melt–fluid (e.g.,  $Sn > 30$  ppm and  $Cs > 35$  ppm) usually exhibit  $Nb/Ta$  ratios  $< 5$  [9], which are significantly different from our samples ( $Sn = 2.58–3.72$  ppm,  $Cs = 8.17–13.81$  ppm, and  $Nb/Ta > 5$ ; Supplementary Table S3; Figure 11a). Therefore, although quartz phenocrysts displaying resorption textures have been observed in the thin section (Figure 2), more evidence, as discussed above, suggests that melt–fluid interaction may not be responsible for the REE tetrad effect in Shiguanshan granite porphyries. These petrographic and geochemical observations enable us to infer that the REE tetrad effect in highly fractionated granites may have been generated before the activity of hydrothermal fluids if granites experienced both magmatic and hydrothermal evolution. On the other hand, the absence of F-rich minerals (such as fluorite) and the presence of high non-chondritic  $Y/Ho$  ratios ( $> 15$ ; Supplementary Table S3) in our samples eliminates the possibility of fluoride–silicate liquid immiscibility in magmatic systems [13,14]. In contrast, it is more plausible that the REE tetrad effect is attributed to fractional crystallization (Figure 11).

As discussed above, excluding melt–fluid interaction and fluoride–silicate liquid immiscibility, the fractionation of accessory minerals is most likely responsible for the REE tetrad effect in the Shiguanshan granite porphyries. This is also supported by mineralogical experiments, that is, the fractionation of accessory minerals such as monazite, xenotime, etc., leads to the REE tetrad effect in granites [15,16]. Based on a rough model of Rayleigh fractionation (see Supplementary Table S4 for formulae and calculations), it appears that the Shiguanshan granite porphyries exhibiting REE tetrad patterns can be most accurately replicated through the separation of plagioclase, K-feldspar, biotite, amphibole, apatite, monazite, and allanite (in a ratio of 40:30:25:4:0.5:0.3:0.2). This fractionation process, with degrees of approximately 20% to 25%, is believed to originate from the parental composition of sample YA16-2-1 from the No-tetrad Yao’an syenite porphyries (Figure 12). Accordingly, the observed REE tetrad effect in highly fractionated granites is likely attributed to the fractionation of accessory minerals, accompanied by the separation of rock-forming min-

erals. The correlation between rare earth element ratios and  $TE_{1,3}$  further supports this conclusion (Figure 7).

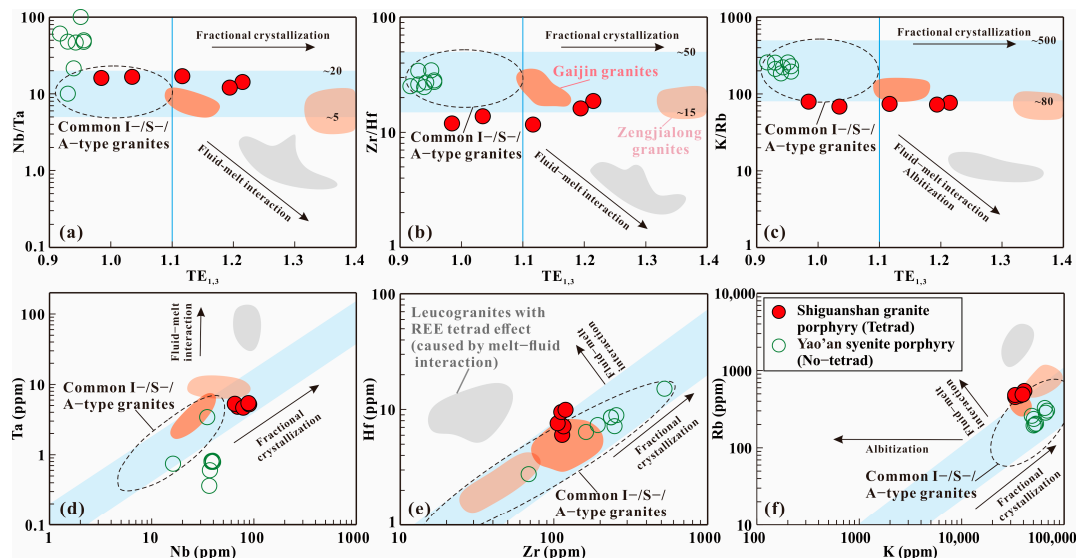


**Figure 11.** (a–c) Plots of Nb/Ta vs.  $TE_{1,3}$ , Zr/Hf vs.  $TE_{1,3}$ , and K/Rb vs.  $TE_{1,3}$  from the Shiguanshan Tetrad granite porphyries and Yao’an No-tetrad syenite porphyries, as well as other granites for comparison, showing decoupling between the REE tetrad effect and fractionation of twin-elements. (d–f) Plots of Ta vs. Nb, Hf vs. Zr, and Rb vs. K. The original diagrams are after Shuai et al. [83], the leucogranites are from Dostal et al. [11], and the Gaijin and Zengjialong granites are from Shuai et al. [83] and Chen et al. [95], respectively.

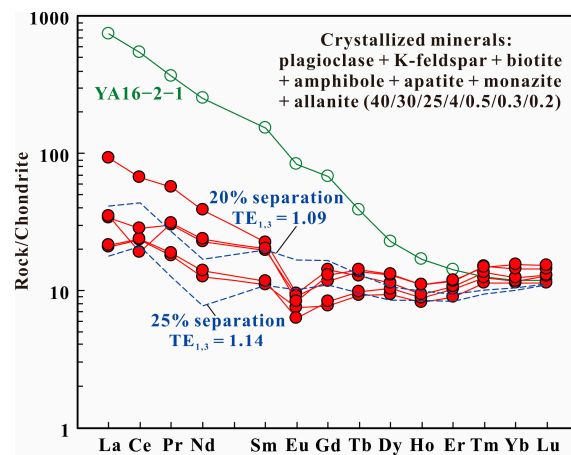


**Figure 12.** Rayleigh modeling results of REE patterns. Sample YA16-2-1, with the lowest  $SiO_2$  from the Yao’an No-tetrad syenite porphyry [61], is assumed to represent the parental magma composition. The partition coefficients of REEs are from Mahood and Hildreth [96], Ward et al. [97], Stepanov et al. [15], and Shimizu et al. [98]. Partitioning coefficients, the fractionated mineral assemblage, and modeling results are listed in Supplementary Table S4b,d.

#### 5.4. Implications of Tectonic Setting

A-type granites crystallize from relatively high-temperature magmas and occur in extensional (rift, plume or hotspot, or post-collisional) settings [81]. This high melting temperature can be realized by the emplacement of mantle-derived mafic magma or upwelling of the asthenosphere [99]. These processes may be achieved through the break-off of a subducted slab or delamination of thickened lithosphere, or convective removal of the lower lithospheric mantle [100].

As discussed above, the Shiguanshan A-type granite porphyry was emplaced at  $34.0 \pm 0.3$  Ma, coinciding with the ages of the Yao'an syenite porphyries and adjacent adakite-like granites and mafic rocks in western Yunnan (Figure 1b). These magmatic suites were emplaced in a post-collisional setting, as geological events following the collision (ca. 60 Ma) [43] of the Indian and Asian plates are referred to as “post-collision” [101]. This is consistent with previous interpretations that they are spatially distant from contemporary subduction zones [20,102]. Therefore, Eocene A-type granites should not be associated with the break-off of a subducted slab but must be related to another tectonic regime. The absence of coeval and direct asthenosphere-derived mafic magmas along the Jinshajiang–Ailaoshan belt, suggesting that the complete removal of the mantle lithosphere perhaps might not have occurred in the western Yangtze Craton [26]. Alternatively, the generation of the Shiguanshan granite porphyries is more likely responsible for the convective removal of the mantle lithosphere from below, and this process leads to an upwelling of hot asthenospheric mantle, causing a thermal anomaly, which in turn leads to partial melting of lithospheric mantle, resulting in the formation of mafic melts. The fractionation of mafic magmas, then, formed the shoshonitic felsic intrusions (e.g., the Yao'an syenite porphyries). The ultimate high-level fractionation of the Yao'an syenite porphyries may result in the generation of highly fractionated A-type granite porphyries in the Shiguanshan. This plausible mechanism for triggering melting of lithospheric mantle is consistent with previous interpretations [18,103]. The presence of post-collisional A-type granite porphyries, therefore, provides new evidence for triggering melting of lithospheric mantle through asthenosphere upwelling induced by convective removal of lithospheric mantle beneath the western Yangtze Craton.

## 6. Conclusions

- (1) The Shiguanshan granite porphyries were emplaced at  $34.0 \pm 0.3$  Ma, which coeval with those of the extensive Eocene–Oligocene felsic and mafic rocks identified in western Yunnan, belonging to the post-collisional magmatic event.
- (2) The Shiguanshan granite porphyries are high-silica and strongly peraluminous, have high DI and zircon saturation temperatures and low MgO, and belong to highly fractionated A-type granites, which likely formed by differentiation of the coeval mantle-derived syenite porphyries. They are likely produced by the fractional crystallization process of a mineral assemblage comprising plagioclase, K-feldspar, biotite, and amphibole (in a ratio of 40:30:25:5), with fractionation degrees of 50%–55%.
- (3) The REE tetrad effect in the Shiguanshan granite porphyries can be attributed to the fractionation of accessory minerals (apatite, allanite, and monazite).
- (4) The primary magma source for the Shiguanshan granite porphyries was derived from enriched lithospheric mantle. The convective removal of the mantle lithosphere can lead to the upwelling of the asthenosphere, which in turn acts as a triggering mechanism for the formation of Shiguanshan A-type granite porphyries by providing the necessary high-melting temperature.

**Supplementary Materials:** The following supporting information can be downloaded at <https://www.mdpi.com/article/10.3390/min13111390/s1>: Table S1: LA-ICP-MS U-Pb data for zircon from the Shiguanshan highly fractionated granite porphyry (SGS-7) in the western Yunnan. Table S2: LA-ICP-MS trace elemental data for zircon from the Shiguanshan highly fractionated granite porphyry (SGS-7) in the western Yunnan. Table S3: Whole-rock major and trace element data for the Shiguanshan granite porphyry and Yao'an syenite porphyry in the western Yunnan. Table S4: The mineral compositions and partition coefficients used for quantitative modeling of fractional crystallization.

**Author Contributions:** Conceptualization, H.Y. and P.W.; methodology, H.Y. and A.L.; software, H.Y.; validation, H.Y. and P.W.; formal analysis, H.Y. and A.L.; investigation, H.Y., P.W., A.L. and F.W.; resources, P.W. and A.L.; data curation, H.Y. and F.W.; writing—original draft preparation, H.Y.; writing—review and editing, P.W. and A.L.; visualization, H.Y.; supervision, F.W.; project administration, P.W. and A.L.; funding acquisition, P.W. and A.L. All authors have read and agreed to the published version of the manuscript.

**Funding:** This study was jointly supported by the National Natural Science Foundation of China (42102047, 41102049), the Yunnan Ten Thousand Talents Plan Young & Elite Talents Project (YNWR-QNBJ-2018-272), the YM Lab Project (2011), and the Innovation Team of Yunnan Province (2012).

**Data Availability Statement:** All data are contained within this article and Supplementary Materials.

**Acknowledgments:** We thank the anonymous reviewers for their constructive comments and suggestions.

**Conflicts of Interest:** The authors declare no conflict of interest.

## References

1. Wu, F.Y.; Liu, X.C.; Liu, Z.C.; Wang, R.C.; Xie, L.; Wang, J.M.; Ji, W.Q.; Yang, L.; Liu, C.; Khanal, G.P.; et al. Highly fractionated Himalayan leucogranites and associated rare-metal mineralization. *Lithos* **2020**, *352–353*, 105319. [\[CrossRef\]](#)
2. Chen, Y.J.; Chen, B.; Duan, X.X.; Sun, H. Origin of highly fractionated peraluminous granites in South China: Implications for crustal anatexis and evolution. *Lithos* **2021**, *402–403*, 106145. [\[CrossRef\]](#)
3. Chappell, B.W.; White, A.J.R. I- and S-type granites in the Lachlan Fold Belt. *Trans. R. Soc. Edinb. Earth Sci.* **1992**, *83*, 1–26. [\[CrossRef\]](#)
4. Wang, R.C.; Wu, F.Y.; Xie, L.; Liu, X.C.; Wang, J.M.; Yang, L.; Lai, W.; Liu, C. A preliminary study of rare-metal mineralization in the Himalayan leucogranite belts, South Tibet. *Sci. China Earth Sci.* **2017**, *60*, 1655–1663. [\[CrossRef\]](#)
5. Wu, F.Y.; Liu, X.C.; Ji, W.Q.; Wang, J.M.; Yang, L. Highly fractionated granites: Recognition and research. *Sci. China Earth Sci.* **2017**, *60*, 1201–1219. [\[CrossRef\]](#)
6. Lee, C.A.; Morton, D.M. High silica granites: Terminal porosity and crystal settling in shallow magma chambers. *Earth Planet. Sci. Lett.* **2015**, *409*, 23–31. [\[CrossRef\]](#)
7. Chen, J.Y.; Yang, J.H.; Zhang, J.H.; Sun, J.F.; Zhu, Y.S.; Hartung, E. Generation of Cretaceous high-silica granite by complementary crystal accumulation and silicic melt extraction in the coastal region of southeastern China. *Geol. Soc. Am. Bull.* **2022**, *134*, 201–222. [\[CrossRef\]](#)
8. Pérez-Soba, C.; Villaseca, C. Petrogenesis of highly fractionated I-type peraluminous granites: La Pedriza pluton (Spanish Central System). *Geol. Acta* **2010**, *8*, 131–149. [\[CrossRef\]](#)
9. Ballouard, C.; Poujol, M.; Boulvais, P.; Branquet, Y.; Tartèse, R.; Vigneresse, J.L. Nb-Ta fractionation in peraluminous granites: A marker of the magmatic-hydrothermal transition. *Geology* **2016**, *44*, 231–234. [\[CrossRef\]](#)
10. Irber, W. The lanthanide tetrad effect and its correlation with K/Rb, Eu/Eu\*, Sr/Eu, Y/Ho, and Zr/Hf of evolving peraluminous granite suites. *Geochim. Cosmochim. Acta* **1999**, *63*, 489–508. [\[CrossRef\]](#)
11. Dostal, J.; Kontak, D.J.; Gerel, O.; Gregory Shellnutt, J.; Fayek, M. Cretaceous ongonites (topaz-bearing albite-rich microleucogranites) from Ongon Khairkhan, Central Mongolia: Products of extreme magmatic fractionation and pervasive metasomatic fluid: Rock interaction. *Lithos* **2015**, *236–237*, 173–189. [\[CrossRef\]](#)
12. Ballouard, C.; Massuyeau, M.; Elburg, M.A.; Tappe, S.; Viljoen, F.; Brandenburg, J.T. The magmatic and magmatic-hydrothermal evolution of felsic igneous rocks as seen through Nb-Ta geochemical fractionation, with implications for the origins of rare-metal mineralizations. *Earth Sci. Rev.* **2020**, *203*, 103115. [\[CrossRef\]](#)
13. Veksler, I.V.; Dorfman, A.M.; Kamenetsky, M.; Dulski, P.; Dingwell, D.B. Partitioning of lanthanides and Y between immiscible silicate and fluoride melts, fluorite and cryolite and the origin of the lanthanide tetrad effect in igneous rocks. *Geochim. Cosmochim. Acta* **2005**, *69*, 2847–2860. [\[CrossRef\]](#)
14. Peretyazhko, I.S.; Savina, E.A. Tetrad effects in the rare earth element patterns of granitoid rocks as an indicator of fluoride—Silicate liquid immiscibility in magmatic systems. *Petrology* **2010**, *18*, 514–543. [\[CrossRef\]](#)
15. Stepanov, A.S.; Hermann, J.; Rubatto, D.; Rapp, R.P. Experimental study of monazite/melt partitioning with implications for the REE, Th and U geochemistry of crustal rocks. *Chem. Geol.* **2012**, *300–301*, 200–220. [\[CrossRef\]](#)
16. Duc-Tin, Q.; Keppeler, H. Monazite and xenotime solubility in granitic melts and the origin of the lanthanide tetrad effect. *Contrib. Mineral. Petrol.* **2015**, *169*, 8. [\[CrossRef\]](#)
17. Wang, J.H.; Yin, A.; Harrison, T.M.; Grove, M.; Zhang, Y.Q.; Xie, G.H. A tectonic model for Cenozoic igneous activities in the eastern Indo-Asian collision zone. *Earth Planet. Sci. Lett.* **2001**, *188*, 123–133. [\[CrossRef\]](#)
18. Hou, Z.Q.; Gao, Y.F.; Qu, X.M.; Rui, Z.Y.; Mo, X.X. Origin of adakitic intrusives generated during mid-Miocene east-west extension in southern Tibet. *Earth Planet. Sci. Lett.* **2004**, *220*, 139–155. [\[CrossRef\]](#)
19. Lu, Y.J.; Kerrich, R.; Cawood, P.A.; McCuaig, T.C.; Hart, C.J.R.; Li, Z.X.; Hou, Z.Q.; Bagas, L. Zircon SHRIMP U-Pb geochronology of potassic felsic intrusions in western Yunnan, SW China: Constraints on the relationship of magmatism to the Jinsha suture. *Gondwana Res.* **2012**, *22*, 737–747. [\[CrossRef\]](#)

20. Lu, Y.J.; McCuaig, T.C.; Li, Z.X.; Jourdan, F.; Hart, C.J.R.; Hou, Z.Q.; Tang, S.H. Paleogene post-collisional lamprophyres in western Yunnan, western Yangtze Craton: Mantle source and tectonic implications. *Lithos* **2015**, *233*, 139–161. [[CrossRef](#)]
21. Hou, Z.Q.; Zhou, Y.; Wang, R.; Zheng, Y.C.; He, W.Y.; Zhao, M.; Weinberg, R.F. Recycling of metal-fertilized lower continental crust: Origin of non-arc Au-rich porphyry deposits at cratonic edges. *Geology* **2017**, *45*, 563–566. [[CrossRef](#)]
22. Shen, Y.; Zheng, Y.C.; Hou, Z.Q.; Zhang, A.P.; Huizenga, J.M.; Wang, Z.X.; Wang, L. Petrology of the Machangqing complex in southeastern Tibet: Implications for the Genesis of potassium-rich adakite-like intrusions in collisional zones. *J. Petrol.* **2021**, *62*, egab066. [[CrossRef](#)]
23. Lu, Y.J.; Kerrich, R.; Kemp, A.I.S.; McCuaig, T.C.; Hou, Z.Q.; Hart, C.J.R.; Li, Z.X.; Cawood, P.A.; Bagas, L.; Yang, Z.M.; et al. Intracontinental Eocene-Oligocene porphyry Cu mineral systems of Yunnan, western Yangtze Craton, China: Compositional characteristics, sources, and implications for continental collision metallogeny. *Econ. Geol.* **2013**, *108*, 1541–1576. [[CrossRef](#)]
24. Chang, J.; Audétat, A. Post-subduction porphyry Cu magmas in the Sanjiang region of southwestern China formed by fractionation of lithospheric mantle-derived mafic magmas. *Geology* **2023**, *51*, 64–68. [[CrossRef](#)]
25. Guo, Z.F.; Hertogen, J.A.N.; Liu, J.Q.; Pasteels, P.; Boven, A.; Punzalan, L.E.A.; He, H.Y.; Luo, X.J.; Zhang, W.H. Potassic Magmatism in Western Sichuan and Yunnan Provinces, SE Tibet, China: Petrological and geochemical constraints on petrogenesis. *J. Petrol.* **2005**, *46*, 33–78. [[CrossRef](#)]
26. Huang, X.L.; Niu, Y.L.; Xu, Y.G.; Chen, L.L.; Yang, Q.J. Mineralogical and geochemical constraints on the petrogenesis of post-collisional potassic and ultrapotassic rocks from Western Yunnan, SW China. *J. Petrol.* **2010**, *51*, 1617–1654. [[CrossRef](#)]
27. Yin, A.; Harrison, T.M. Geologic evolution of the Himalayan-Tibetan Orogen. *Annu. Rev. Earth Planet. Sci.* **2000**, *28*, 211–280. [[CrossRef](#)]
28. Leech, M.L.; Singh, S.; Jain, A.K.; Klemperer, S.L.; Manickavasagam, R.M. The onset of India-Asia continental collision: Early, steep subduction required by the timing of UHP metamorphism in the western Himalaya. *Earth Planet. Sci. Lett.* **2005**, *234*, 83–97. [[CrossRef](#)]
29. Zhu, D.C.; Zhao, Z.D.; Niu, Y.; Dilek, Y.; Hou, Z.Q.; Mo, X.X. The origin and pre-Cenozoic evolution of the Tibetan Plateau. *Gondwana Res.* **2013**, *23*, 1429–1454. [[CrossRef](#)]
30. Deng, J.; Wang, Q.F.; Li, G.J.; Santosh, M. Cenozoic tectono-magmatic and metallogenic processes in the Sanjiang region, southwestern China. *Earth Sci. Rev.* **2014**, *138*, 268–299. [[CrossRef](#)]
31. Metcalfe, I. Gondwana dispersion and Asian accretion: Tectonic and palaeogeographic evolution of eastern Tethys. *J. Asian Earth Sci.* **2013**, *66*, 1–33. [[CrossRef](#)]
32. Zhao, J.H.; Zhou, M.F.; Yan, D.P.; Zheng, J.P.; Li, J.W. Reappraisal of the ages of Neoproterozoic strata in South China: No connection with the Grenvillian orogeny. *Geology* **2011**, *39*, 299–302. [[CrossRef](#)]
33. Cawood, P.A.; Zhao, G.C.; Yao, J.L.; Wang, W.; Xu, Y.J.; Wang, Y.J. Reconstructing South China in Phanerozoic and Precambrian supercontinents. *Earth Sci. Rev.* **2018**, *186*, 173–194. [[CrossRef](#)]
34. Zhou, M.F.; Yan, D.P.; Kennedy, A.K.; Li, Y.Q.; Ding, J. SHRIMP zircon U-Pb geochronological and geochemical evidence for Neoproterozoic arc-related magmatism along the western margin of the Yangtze Block, South China. *Earth Planet. Sci. Lett.* **2002**, *196*, 51–67. [[CrossRef](#)]
35. Dong, Y.P.; Liu, X.M.; Santosh, M.; Zhang, X.N.; Chen, Q.; Yang, C.; Yang, Z. Neoproterozoic subduction tectonics of the northwestern Yangtze Block in South China: Constrains from zircon U-Pb geochronology and geochemistry of mafic intrusions in the Hannan Massif. *Precambrian Res.* **2011**, *189*, 66–90. [[CrossRef](#)]
36. Li, Z.X.; Evans, D.A.D.; Halverson, G.P. Neoproterozoic glaciations in a revised global palaeogeography from the breakup of Rodinia to the assembly of Gondwanaland. *Sedimentary Geol.* **2013**, *294*, 219–232. [[CrossRef](#)]
37. Dong, Y.P.; Liu, X.M.; Santosh, M.; Chen, Q.; Zhang, X.N.; Li, W.; He, D.F.; Zhang, G.W. Neoproterozoic accretionary tectonics along the northwestern margin of the Yangtze Block, China: Constraints from zircon U-Pb geochronology and geochemistry. *Precambrian Res.* **2012**, *196–197*, 247–274. [[CrossRef](#)]
38. Zhao, J.H.; Li, Q.W.; Liu, H.; Wang, W. Neoproterozoic magmatism in the western and northern margins of the Yangtze Block (South China) controlled by slab subduction and subduction-transform edge propagator. *Earth Sci. Rev.* **2018**, *187*, 1–18. [[CrossRef](#)]
39. Zhang, Z.C.; Mahoney, J.J.; Mao, J.W.; Wang, F.S. Geochemistry of picritic and associated basalt flows of the Western Emeishan Flood Basalt Province. *J. Petrol.* **2006**, *47*, 1997–2019. [[CrossRef](#)]
40. Jian, P.; Liu, D.Y.; Kröner, A.; Zhang, Q.; Wang, Y.Z.; Sun, X.M.; Zhang, W. Devonian to Permian plate tectonic cycle of the Paleo-Tethys Orogen in southwest China (II): Insights from zircon ages of ophiolites, arc/back-arc assemblages and within-plate igneous rocks and generation of the Emeishan CFB province. *Lithos* **2009**, *113*, 767–784. [[CrossRef](#)]
41. Mo, X.X.; Deng, J.F.; Lu, F.X. Volcanism and the evolution of Tethys in Sanjiang area, southwestern China. *J. SE Asian Earth Sci.* **1994**, *9*, 325–333. [[CrossRef](#)]
42. Wang, X.F.; Metcalfe, I.; Jian, P.; He, L.Q.; Wang, C.S. The Jinshajiang-Ailaoshan Suture zone, China: Tectonostratigraphy, age and evolution. *J. Asian Earth Sci.* **2000**, *18*, 675–690. [[CrossRef](#)]
43. Chung, S.L.; Chu, M.F.; Zhang, Y.Q.; Xie, Y.W.; Lo, C.H.; Lee, T.Y.; Lan, C.Y.; Li, X.H.; Zhang, Q.; Wang, Y.Z. Tibetan tectonic evolution inferred from spatial and temporal variations in post-collisional magmatism. *Earth Sci. Rev.* **2005**, *68*, 173–196. [[CrossRef](#)]
44. Campbell, I.H.; Stepanov, A.S.; Liang, H.Y.; Allen, C.M.; Norman, M.D.; Zhang, Y.Q.; Xie, Y.W. The origin of shoshonites: New insights from the Tertiary high-potassium intrusions of eastern Tibet. *Contrib. Mineral. Petrol.* **2014**, *167*, 983–1004. [[CrossRef](#)]

45. Hu, Z.C.; Li, X.H.; Luo, T.; Zhang, W.; Crowley, J.; Li, Q.L.; Ling, X.X.; Yang, C.; Li, Y.; Feng, L.P.; et al. Tanz zircon megacrysts: A new zircon reference material for the microbeam determination of U-Pb ages and Zr-O isotopes. *J. Anal. At. Spectrom.* **2021**, *36*, 2715–2734. [[CrossRef](#)]
46. Zong, K.Q.; Klemm, R.; Yuan, Y.; He, Z.Y.; Guo, J.L.; Shi, X.L.; Liu, Y.S.; Hu, Z.C.; Zhang, Z.M. The assembly of Rodinia: The correlation of early Neoproterozoic (ca. 900 Ma) high-grade metamorphism and continental arc formation in the southern Beishan Orogen, southern Central Asian Orogenic Belt (CAOB). *Precambrian Res.* **2017**, *290*, 32–48. [[CrossRef](#)]
47. Liu, Y.S.; Gao, S.; Hu, Z.C.; Gao, C.G.; Zong, K.Q.; Wang, D.B. Continental and oceanic crust recycling-induced melt-peridotite interactions in the Trans-North China Orogen: U-Pb dating, Hf isotopes and trace elements in zircons of mantle xenoliths. *J. Petrol.* **2010**, *51*, 537–571. [[CrossRef](#)]
48. Ludwig, K.R. *ISOPLLOT 3.00: A Geochronological Toolkit for Microsoft Excel*; Berkeley Geochronology Center Special Publication No 4; Berkeley Geochronology Center: Berkeley, CA, USA, 2003.
49. Hu, Z.C.; Liu, Y.S.; Gao, S.; Liu, W.G.; Zhang, W.; Tong, X.R.; Lin, L.; Zong, K.Q.; Li, M.; Chen, H.H.; et al. Improved in situ Hf isotope ratio analysis of zircon using newly designed X-skimmer cone and jet sample cone in combination with the addition of nitrogen by laser ablation multiple collector ICP-MS. *J. Anal. At. Spectrom.* **2012**, *27*, 1391–1399. [[CrossRef](#)]
50. Qi, L.; Hu, J.; Gregoire, D.C. Determination of trace elements in granites by inductively coupled plasma mass spectrometry. *Talanta* **2000**, *51*, 507–513. [[CrossRef](#)]
51. Lin, J.; Liu, Y.S.; Yang, Y.H.; Hu, Z.C. Calibration and correction of LA-ICP-MS and LA-MC-ICP-MS analyses for element contents and isotopic ratios. *Solid Earth Sci.* **2016**, *1*, 5–27. [[CrossRef](#)]
52. Zhang, W.; Hu, Z.C. Estimation of isotopic reference values for pure materials and geological reference materials. *Atomic Spectroscopy* **2020**, *41*, 93–102. [[CrossRef](#)]
53. Li, C.F.; Li, X.H.; Li, Q.L.; Guo, J.H.; Li, X.H.; Yang, Y.H. Rapid and precise determination of Sr and Nd isotopic ratios in geological samples from the same filament loading by thermal ionization mass spectrometry employing a single-step separation scheme. *Anal. Chim. Acta* **2012**, *727*, 54–60. [[CrossRef](#)]
54. Hoskin, P.W.O.; Schaltegger, U. The composition of zircon and igneous and metamorphic petrogenesis. *Rev. Mineral. Geochem.* **2003**, *53*, 27–62. [[CrossRef](#)]
55. Hoskin, P.W.O. Trace-element composition of hydrothermal zircon and the alteration of Hadean zircon from the Jack Hills, Australia. *Geochim. Cosmochim. Acta* **2005**, *69*, 637–648. [[CrossRef](#)]
56. Sun, S.S.; McDonough, W.F. Chemical and isotopic systematics of oceanic basalts: Implications for mantle composition and processes. *Geol. Soc. Lond. Spec. Publ.* **1989**, *42*, 313–345. [[CrossRef](#)]
57. Middlemost, E.A.K. Naming materials in the magma/igneous rock system. *Earth Sci. Rev.* **1994**, *37*, 215–224. [[CrossRef](#)]
58. Peccerillo, A.; Taylor, S.R. Geochemistry of Eocene calc-alkaline volcanic rocks from the Kastamonu area, northern Turkey. *Contrib. Mineral. Petrol.* **1976**, *58*, 63–81. [[CrossRef](#)]
59. Maniar, P.D.; Piccoli, P.M. Tectonic discrimination of granitoids. *Geol. Soc. Am. Bull.* **1989**, *101*, 635–643. [[CrossRef](#)]
60. Bouseily, A.M.E.; Sokkary, A.A.E. The relation between Rb, Ba and Sr in granitic rocks. *Chem. Geol.* **1975**, *16*, 207–219. [[CrossRef](#)]
61. Luo, C.H.; Zhou, Y.; Shen, Y. The geochemical characteristics and petrogenesis of the mineralized alkali-rich magmatic rock in Yao'an Au-Pb-Ag deposit, Yunnan province. *Earth Sci.* **2019**, *44*, 2063–2083, (In Chinese with English Abstract). [[CrossRef](#)]
62. Xu, X.S.; Qiu, J.S. *Igneous Petrology*; Science Press: Beijing, China, 2010; pp. 1–346. (In Chinese)
63. Nash, W.P.; Crecraft, H.R. Partition coefficients for trace elements in silicic magmas. *Geochim. Cosmochim. Acta* **1985**, *49*, 2309–2322. [[CrossRef](#)]
64. Tiepolo, M.; Oberti, R.; Zanetti, A.; Vannucci, R.; Foley, S.F. Trace-element partitioning between amphibole and silicate melt. *Rev. Mineral. Geochem.* **2007**, *67*, 417–452. [[CrossRef](#)]
65. Jacobsen, S.B.; Wasserburg, G.J. Sm-Nd isotopic evolution of chondrites. *Earth Planet. Sci. Lett.* **1980**, *50*, 139–155. [[CrossRef](#)]
66. Goldstein, S.L.; O'Nions, R.K.; Hamilton, P.J. A Sm-Nd isotopic study of atmospheric dusts and particulates from major river systems. *Earth Planet. Sci. Lett.* **1984**, *70*, 221–236. [[CrossRef](#)]
67. Peucat, J.J.; Vidal, P.; Bernard-Griffiths, J.; Condie, K.C. Sr, Nd, and Pb isotopic systematics in the Archean low- to high-grade transition zone of southern India: Syn-accretion vs. post-accretion granulites. *J. Geol.* **1989**, *97*, 537–549. [[CrossRef](#)]
68. Steiger, R.H.; Jäger, E. Subcommittee on geochronology: Convention on the use of decay constants in geo- and cosmochronology. *Earth Planet. Sci. Lett.* **1977**, *36*, 359–362. [[CrossRef](#)]
69. Lugmair, G.W.; Marti, K. Lunar initial  $^{143}\text{Nd}/^{144}\text{Nd}$ : Differential evolution of the lunar crust and mantle. *Earth Planet. Sci. Lett.* **1978**, *39*, 349–357. [[CrossRef](#)]
70. He, W.Y.; Mo, X.X.; Yang, L.Q.; Xing, Y.L.; Dong, G.C.; Yang, Z.; Gao, X.; Bao, X.S. Origin of the Eocene porphyries and mafic microgranular enclaves from the Beiya porphyry Au polymetallic deposit, western Yunnan, China: Implications for magma mixing/mingling and mineralization. *Gondwana Res.* **2016**, *40*, 230–248. [[CrossRef](#)]
71. Yan, Q.G.; Jiang, X.J.; Li, C.; Zhou, L.M.; Wang, Z.Q.; Sultan, B.S.; Qu, W.J.; Du, A.D. Geodynamic background of intracontinental Cenozoic alkaline volcanic rocks in Laojiezi, western Yangtze Craton: Constraints from Sr-Nd-Hf-O isotopes. *Acta Geol. Sin.* **2018**, *92*, 2098–2119.
72. Yan, Q.G.; Guo, Z.L.; Li, C.; Jiang, X.J.; Wang, Z.Q.; Li, Y.D. Zircon LA-ICP-MS U-Pb geochronology and Hf isotopes of lamprophyre in Gan'gou gold deposit, Yao'an County, Central Yunnan Province. *Miner. Depos.* **2019**, *38*, 526–540, (In Chinese with English Abstract). [[CrossRef](#)]

73. Blichert-Toft, J.; Albarède, F. The Lu-Hf isotope geochemistry of chondrites and the evolution of the mantle–crust system. *Earth Planet. Sci. Lett.* **1997**, *148*, 243–258. [[CrossRef](#)]
74. Griffin, W.L.; Pearson, N.J.; Belousova, E.; Jackson, S.E.; van Achterbergh, E.; O'Reilly, S.Y.; Shee, S.R. The Hf isotope composition of cratonic mantle: LAM-MC-ICPMS analysis of zircon megacrysts in kimberlites. *Geochim. Cosmochim. Acta* **2000**, *64*, 133–147. [[CrossRef](#)]
75. Söderlund, U.; Patchett, P.J.; Vervoort, J.D.; Isachsen, C.E. The  $^{176}\text{Lu}$  decay constant determined by Lu-Hf and U-Pb isotope systematics of Precambrian mafic intrusions. *Earth Planet. Sci. Lett.* **2004**, *219*, 311–324. [[CrossRef](#)]
76. Griffin, W.L.; Wang, X.; Jackson, S.E.; Pearson, N.J.; O'Reilly, S.Y.; Xu, X.S.; Zhou, X.M. Zircon chemistry and magma mixing, SE China: In-situ analysis of Hf isotopes, Tonglu and Pingtan igneous complexes. *Lithos* **2002**, *61*, 237–269. [[CrossRef](#)]
77. Chappell, B.W.; White, A.J.R. Two contrasting granite types: 25 years later. *Aust. J. Earth Sci.* **2001**, *48*, 489–499. [[CrossRef](#)]
78. Wu, F.Y.; Li, X.H.; Yang, J.H.; Zheng, Y.F. Discussions on the petrogenesis of granites. *Acta Petrol. Sin.* **2007**, *23*, 1217–1238, (In Chinese with English Abstract).
79. Watson, E.B.; Harrison, T.M. Zircon saturation revisited: Temperature and composition effects in a variety of crustal magma types. *Earth Planet. Sci. Lett.* **1983**, *64*, 295–304. [[CrossRef](#)]
80. Miller, C.F.; McDowell, S.M.; Mapes, R.W. Hot and cold granites? Implications of zircon saturation temperatures and preservation of inheritance. *Geology* **2003**, *31*, 529–532. [[CrossRef](#)]
81. Eby, G. Chemical subdivision of the A-type granitoids: Petrogenetic and tectonic implication. *Geology* **1992**, *20*, 641–644. [[CrossRef](#)]
82. Whalen, J.B.; Currie, K.L.; Chappell, B.W. A-type granites: Geochemical characteristics, discrimination and petrogenesis. *Contrib. Mineral. Petrol.* **1987**, *95*, 407–419. [[CrossRef](#)]
83. Shuai, X.; Li, S.M.; Zhu, D.C.; Wang, Q.; Zhang, L.L.; Zhao, Z.D. Tetrad effect of rare earth elements caused by fractional crystallization in high-silica granites: An example from central Tibet. *Lithos* **2021**, 384–385, 105968. [[CrossRef](#)]
84. Landenberger, B.; Collins, W.J. Derivation of A-type granites from a dehydrated charnockitic lower crust: Evidence from the Chaelundi Complex, eastern Australia. *J. Petrol.* **1996**, *37*, 145–170. [[CrossRef](#)]
85. Zhu, R.Z.; Lai, S.C.; Fowler, M.; Xie, J.C.; Glynn, S.M. A microcosm of modern crust formation: Evidence from zircon ages, Hf-O and Nd-Sr isotopes and bulk geochemistry of the Menglian Batholith, SE Tibet. *Chem. Geol.* **2023**, *618*, 121276. [[CrossRef](#)]
86. Turner, S.P.; Foden, J.D.; Morrison, R.S. Derivation of some A-type magmas by fractionation of basaltic magma: An example from the Padthaway Ridge, South Australia. *Lithos* **1992**, *28*, 151–179. [[CrossRef](#)]
87. Litvinovsky, B.A.; Jahn, B.M.; Zangvilovich, A.N.; Saunders, A.; Poulain, S.; Kuzmin, D.V.; Reichow, M.K.; Titov, A.V. Petrogenesis of syenite–granite suites from the Bryansky Complex (Transbaikalia, Russia): Implications for the origin of A-type granitoid magmas. *Chem. Geol.* **2002**, *16*, 105–133. [[CrossRef](#)]
88. Baker, M.B.; Hirschmann, M.M.; Ghiorso, M.S.; Stolper, E.M. Compositions of near-solidus predictive melts from experiments and thermodynamic calculations. *Nature* **1995**, *375*, 308–311. [[CrossRef](#)]
89. Woodhead, J.; Hergt, J.; Greig, A.; Edwards, L. Subduction zone Hf-anomalies: Mantle messenger, melting artefact or crustal process? *Earth Planet. Sci. Lett.* **2011**, *304*, 231–239. [[CrossRef](#)]
90. Li, X.; Li, W.; Wang, X.; Li, Q.; Liu, Y.; Tang, G. Role of mantle-derived magma in genesis of early Yanshanian granites in the Nanling Range, South China: In situ zircon Hf–O isotopic constraints. *Sci. China Earth Sci.* **2009**, *52*, 1262–1278. [[CrossRef](#)]
91. Bau, M. Controls on the fractionation of isovalent trace elements in magmatic and aqueous systems: Evidence from Y/Ho, Zr/Hf, and lanthanide tetrad effect. *Contrib. Mineral. Petrol.* **1996**, *123*, 323–333. [[CrossRef](#)]
92. Monecke, T.; Kempe, U.; Trinkler, M.; Thomas, R.; Dulski, P.; Wagner, T. Unusual rare earth element fractionation in a tin-bearing magmatic-hydrothermal system. *Geology* **2011**, *39*, 295–298. [[CrossRef](#)]
93. Lee, H.M.; Lee, S.G.; Kim, H.; Lee, J.I.; Lee, M.J. REE tetrad effect and Sr-Nd isotope systematics of A-type Pirrit Hills granite from West Antarctica. *Minerals* **2022**, *11*, 792. [[CrossRef](#)]
94. Stepanov, A.S.; Hermann, J. Fractionation of Nb and Ta by biotite and phengite: Implications for the “missing Nb paradox”. *Geology* **2013**, *41*, 303–306. [[CrossRef](#)]
95. Chen, B.; Gu, H.O.; Chen, Y.; Sun, K.; Chen, W. Lithium isotope behavior during partial melting of metapelites from the Jiangnan Orogen, South China: Implications for the origin of REE tetrad effect of F-rich granite and associated rare-metal mineralization. *Chem. Geol.* **2018**, *483*, 372–384. [[CrossRef](#)]
96. Mahood, G.A.; Hildreth, W. Large partition coefficients for trace elements in high-silica rhyolites. *Geochim. Cosmochim. Acta* **1983**, *47*, 11–30. [[CrossRef](#)]
97. Ward, C.D.; McArthur, J.; Walsh, J.N. Rare earth element behavior during evolution and alteration of the Dartmoor granite, SW England. *J. Petrol.* **1992**, *33*, 785–815. [[CrossRef](#)]
98. Shimizu, K.; Liang, Y.; Sun, C.G.; Jackson, C.R.M.; Saal, A.E. Parameterized lattice strain models for REE partitioning between amphibole and silicate melt. *Am. Mineral.* **2017**, *102*, 2254–2267. [[CrossRef](#)]
99. Wu, F.Y.; Sun, D.Y.; Li, H.M.; Jahn, B.M.; Wilde, S. A-type granites in northeastern China: Age and geochemical constraints on their petrogenesis. *Chem. Geol.* **2002**, *187*, 143–173. [[CrossRef](#)]
100. Whalen, J.B.; Jenner, G.A.; Longstaffe, F.J.; Robert, F.; Gariépy, C. Geochemical and isotopic (O, Nd, Pb and Sr) constraints on A-type granite petrogenesis based on the Topsails igneous suite, Newfoundland Appalachians. *J. Petrol.* **1996**, *37*, 1463–1489. [[CrossRef](#)]

101. Capitanio, F.A.; Morra, G.; Goes, S.; Weinberg, R.F.; Moresi, L. India–Asia convergence driven by the subduction of the Greater Indian continent. *Nature Geosci.* **2010**, *3*, 136–139. [[CrossRef](#)]
102. Hou, Z.Q.; Ma, H.W.; Zaw, K.; Zhang, Y.Q.; Wang, M.J.; Wang, Z.; Pan, G.T.; Tang, R.L. The Himalayan Yulong porphyry copper belt: Product of large-scale strike-slip faulting in eastern Tibet. *Econ. Geol.* **2003**, *98*, 125–145. [[CrossRef](#)]
103. Clemens, J.D. S-type granitic magmas-petrogenetic issues, models and evidence. *Earth Sci. Rev.* **2003**, *61*, 1–18. [[CrossRef](#)]

**Disclaimer/Publisher’s Note:** The statements, opinions and data contained in all publications are solely those of the individual author(s) and contributor(s) and not of MDPI and/or the editor(s). MDPI and/or the editor(s) disclaim responsibility for any injury to people or property resulting from any ideas, methods, instructions or products referred to in the content.